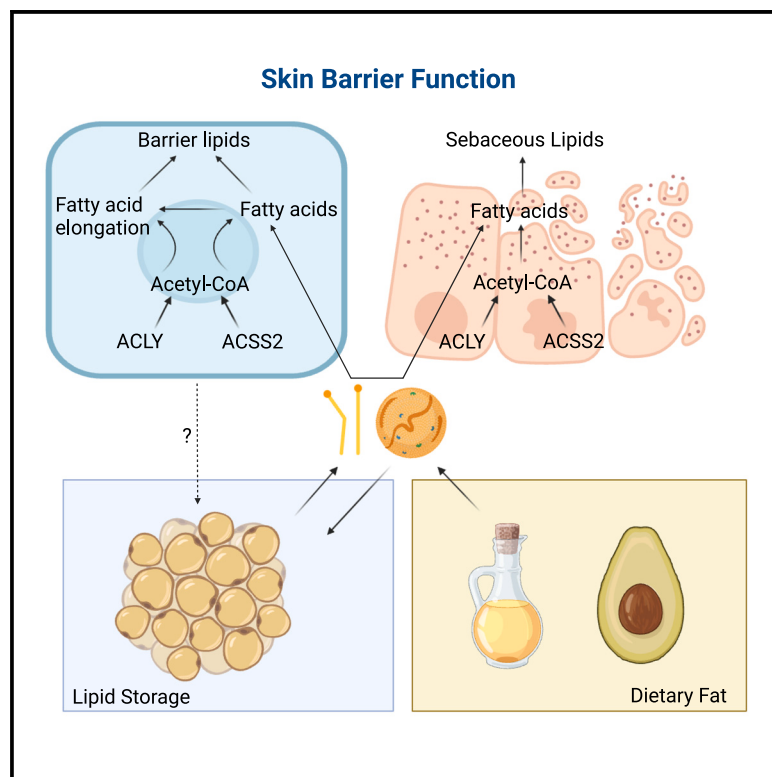


## Acetyl-CoA synthesis in the skin is a key determinant of systemic lipid homeostasis

### Graphical abstract



### Authors

Phuong T.T. Nguyen, Mia Shiue,  
Nina Kuprasertkul, ...,  
Clementina Mesaros, Brian C. Capell,  
Kathryn E. Wellen

### Correspondence

wellenk@upenn.edu

### In brief

Nguyen et al. demonstrate that loss of acetyl-CoA synthesis enzymes in mouse skin depletes key epidermal barrier lipids, disrupts the skin barrier, and causes rapid fat loss. Sebum production is sustained using circulating lipids. These findings reveal the vital role of skin acetyl-CoA synthesis in local and systemic lipid metabolism.

### Highlights

- Systemic deletion of *Acly* in adult mice results in skin abnormalities and fat loss
- *Acly* and *Acss2* loss (DKO) in skin induces barrier dysfunction and adipose lipolysis
- DKO skin exhibits depletion of epidermal barrier lipids but higher sebum production
- Impaired acetyl-CoA synthesis renders the skin highly sensitive to exogenous lipids



## Article

# Acetyl-CoA synthesis in the skin is a key determinant of systemic lipid homeostasis

Fuong T.T. Nguyen,<sup>1,2,3</sup> Mia Shiue,<sup>1,2</sup> Nina Kuprasertkul,<sup>1,2,4,5</sup> Pedro Costa-Pinheiro,<sup>1,2</sup> Luke T. Izzo,<sup>1,2,5</sup> Laura V. Pinheiro,<sup>1,2,6</sup> Hayley A. Affronti,<sup>1,2</sup> Gabriel Gugiu,<sup>7</sup> Shivani Ghaisas,<sup>1,2</sup> Joyce Y. Liu,<sup>1,2,6</sup> Jordan C. Harris,<sup>4,8,9</sup> Charles W. Bradley,<sup>10</sup> John T. Seykora,<sup>4</sup> Xiaolu Yang,<sup>1,2</sup> Taku Kambayashi,<sup>8</sup> Clementina Mesaros,<sup>7</sup> Brian C. Capell,<sup>4</sup> and Kathryn E. Wellen<sup>1,2,11,\*</sup>

<sup>1</sup>Department of Cancer Biology, University of Pennsylvania, Philadelphia, PA, USA

<sup>2</sup>Abramson Family Cancer Research Institute, University of Pennsylvania, Philadelphia, PA, USA

<sup>3</sup>Neuroscience Graduate Group, University of Pennsylvania, Philadelphia, PA, USA

<sup>4</sup>Department of Dermatology, University of Pennsylvania, Philadelphia, PA, USA

<sup>5</sup>Cell and Molecular Biology Graduate Group, University of Pennsylvania, Philadelphia, PA, USA

<sup>6</sup>Biochemistry and Molecular Biophysics Graduate Group, University of Pennsylvania, Philadelphia, PA, USA

<sup>7</sup>Department of Systems Pharmacology and Translational Therapeutics, University of Pennsylvania, Philadelphia, PA, USA

<sup>8</sup>Department of Pathology and Laboratory Medicine, University of Pennsylvania, Philadelphia, PA, USA

<sup>9</sup>Immunology Graduate Group, University of Pennsylvania, Philadelphia, PA, USA

<sup>10</sup>Department of Pathobiology, School of Veterinary Medicine, University of Pennsylvania, Philadelphia, PA, USA

<sup>11</sup>Lead contact

\*Correspondence: wellenk@upenn.edu

<https://doi.org/10.1016/j.celrep.2025.115284>

## SUMMARY

ATP-citrate lyase (ACLY) generates cytosolic acetyl-coenzyme A (acetyl-CoA) for lipid synthesis and is a promising therapeutic target in diseases with altered lipid metabolism. Here, we developed inducible whole-body Acly-knockout mice to determine the requirement for ACLY in normal tissue functions, uncovering its crucial role in skin homeostasis. ACLY-deficient skin upregulates the acetyl-CoA synthetase ACSS2; deletion of both Acly and Acss2 from the skin exacerbates skin abnormalities, with differential effects on two major lipid-producing skin compartments. While the epidermis is depleted of barrier lipids, the sebaceous glands increase production of sebum, supplied at least in part by circulating fatty acids and coinciding with adipose lipolysis and fat depletion. Dietary fat supplementation further boosts sebum production and partially rescues both the lipoatrophy and the aberrant skin phenotypes. The data establish a critical role for cytosolic acetyl-CoA synthesis in maintaining skin barrier integrity and highlight the skin as a key organ in systemic lipid regulation.

## INTRODUCTION

Acetyl-coenzyme A (acetyl-CoA) is a building block for lipids, making its synthesis of interest for therapeutic targeting in diseases with dysregulated lipid metabolism. ATP-citrate lyase (ACLY) generates acetyl-CoA in the cytosol and nucleus from the cleavage of mitochondrion-derived citrate. Alternatively, nucleocytosolic acetyl-CoA can be generated from acetate by acyl-CoA synthetase short-chain family member 2 (ACSS2). This pool of acetyl-CoA provides the two-carbon acetyl moiety for biosynthesis of fatty acids and sterols, as well as for acetylation of histone and non-histone proteins.<sup>1–3</sup> Dysregulation of ACLY has been implicated in fatty liver diseases, dyslipidemia, atherosclerosis, and cancer.<sup>4–6</sup> Bempedoic acid, a pro-drug that is activated in the liver to inhibit ACLY, is in clinical use to treat hypercholesterolemia and cardiovascular diseases.<sup>7,8</sup> In addition, preclinical studies have demonstrated the anticancer effects of abrogating ACLY<sup>9–17</sup> or ACSS2<sup>18–24</sup> in various types of cancer. Given the potential of inhibiting these enzymes sys-

temically for metabolic diseases and cancer, it is imperative to understand their functions in normal tissue homeostasis.

Previous work showed that mice with constitutive knockout of ACSS2 are phenotypically normal on standard chow diet.<sup>25</sup> An ACSS2 inhibitor, MTB-9655, is currently in phase I clinical trial for advanced solid tumors, with pending human safety data.<sup>26</sup> In contrast, constitutive knockout of ACLY in mice is embryonically lethal.<sup>27</sup> Hence, genetic studies of ACLY have been limited to cell- or tissue-specific knockouts (e.g., in adipose tissues,<sup>28–30</sup> liver,<sup>31–34</sup> pancreas,<sup>14</sup> myeloid cells,<sup>35–37</sup> and T cells<sup>38,39</sup>). Many of these models have mild phenotypes under unchallenged conditions, reflecting in part compensatory mechanisms, including upregulation of ACSS2, to supply acetyl-CoA.<sup>28,31,35</sup> However, it remains unclear if there are tissues in the adult organism that require ACLY for normal function.

To interrogate the effects of depleting ACLY at the organismal level, we generated an inducible whole-body knockout of Acly in adult mice. These mice sustain weight loss and fat loss, along with developing dry scaly skin and alopecia. Since ACSS2 is



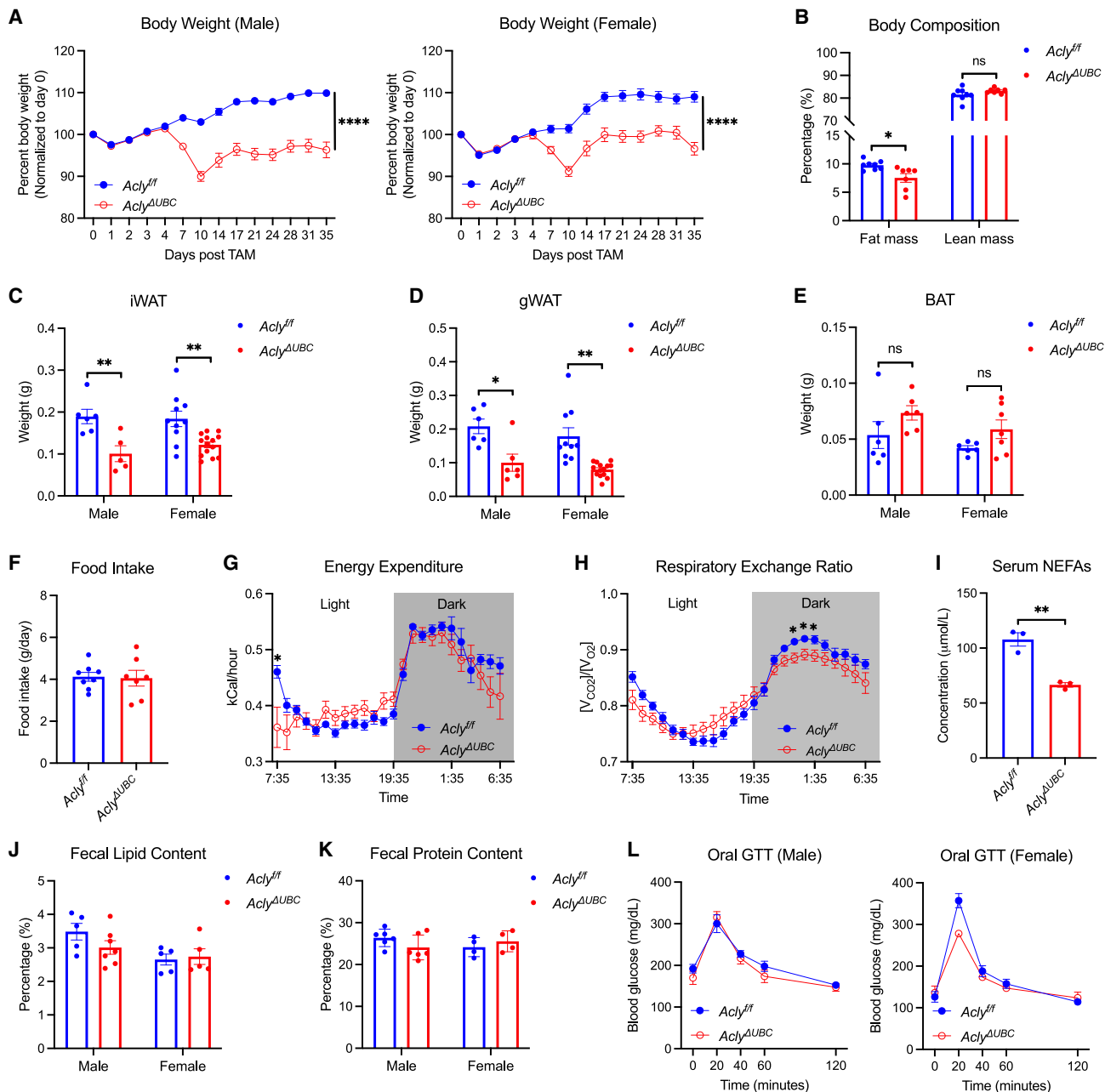


**Figure 1. Whole-body deletion of Acly in adult mice results in fat loss with minimal changes in nutrient consumption or energy expenditure**

(A) Body weight of wild-type ( $\text{Acly}^{\text{ff}}$ ) and whole-body Acly-knockout ( $\text{Acly}^{\text{AUBC}}$ ) mice over 5 weeks post tamoxifen (TAM) induction. Each time point is normalized to day 0 (males,  $n = 45$   $\text{Acly}^{\text{ff}}$ ,  $n = 49$   $\text{Acly}^{\text{AUBC}}$ ; females,  $n = 35$   $\text{Acly}^{\text{ff}}$ ,  $n = 39$   $\text{Acly}^{\text{AUBC}}$ ). (B) Body composition analysis by EchoMRI for male mice ( $\text{Acly}^{\text{ff}}$ ,  $n = 8$ ;  $\text{Acly}^{\text{AUBC}}$ ,  $n = 7$ ) at experimental endpoint. (C–E) Weight of mouse (C) iWAT (males,  $n = 6$   $\text{Acly}^{\text{ff}}$ ,  $n = 5$   $\text{Acly}^{\text{AUBC}}$ ; females,  $n = 10$   $\text{Acly}^{\text{ff}}$ ,  $n = 14$   $\text{Acly}^{\text{AUBC}}$ ), (D) gWAT (males,  $n = 6$   $\text{Acly}^{\text{ff}}$ ,  $n = 6$   $\text{Acly}^{\text{AUBC}}$ ; females,  $n = 10$   $\text{Acly}^{\text{ff}}$ ,  $n = 14$   $\text{Acly}^{\text{AUBC}}$ ), and (E) BAT (males,  $n = 6$   $\text{Acly}^{\text{ff}}$ ,  $n = 6$   $\text{Acly}^{\text{AUBC}}$ ; females,  $n = 6$   $\text{Acly}^{\text{ff}}$ ,  $n = 7$   $\text{Acly}^{\text{AUBC}}$ ). (F–H) Metabolic assessments by Promethion metabolic cage analysis for male mice ( $n = 8$   $\text{Acly}^{\text{ff}}$ ,  $n = 7$   $\text{Acly}^{\text{AUBC}}$ ) over the last 7 days of the experiment, including (F) daily food intake (each data point represents an individual mouse's average daily food intake over 7 days), (G) energy expenditure, and (H) respiratory exchange ratio; for (G) and (H), each data point represents an average of all mice for each genotype. (I) Serum non-esterified fatty acids (NEFAs) ( $\mu\text{mol/L}$ ) in wild-type and  $\text{Acly}^{\text{AUBC}}$  mice fed *ad libitum*, measured by colorimetric assay ( $\text{Acly}^{\text{ff}}$ ,  $n = 3$ ;  $\text{Acly}^{\text{AUBC}}$ ,  $n = 3$ ).

(legend continued on next page)

upregulated in the skin upon loss of ACLY, we generated mice with inducible skin-specific double knockout (DKO) of *Acly* and *Acss2* to study the role of nucleocytosolic acetyl-CoA in skin homeostasis. Loss of both ACLY and ACSS2 in the skin of adult mice exacerbates cutaneous abnormalities and triggers rapid adipose depletion. Dietary lipid supplementation alleviates both skin and adipose phenotypes.

Lipids are crucial components of the skin barrier, which protects organisms against environmental insults and loss of water and body heat. The epidermis is the outermost skin layer and produces specialized lipids, which comprise structural elements of the skin permeability barrier.<sup>40</sup> Distinct from epidermal lipids, sebum lipids produced by the sebaceous glands (SGs) are secreted through hair follicles, coating the skin surface to provide moisturization and antimicrobial properties.<sup>41</sup> In this study, we found that loss of ACLY and ACSS2 in the skin depletes epidermal lipids critical for skin barrier function. In contrast, lipid-rich sebum production is maintained and even modestly increases. Maintenance of sebum coincides with adipose depletion and is also further boosted by dietary lipid supplementation. Together, the data establish the importance of acetyl-CoA-synthesizing enzymes in epidermal and SG lipid metabolism and reveal that impaired acetyl-CoA synthesis within the skin results in rapid depletion of fat stores, positioning the skin as a key contributor to systemic lipid homeostasis.

## RESULTS

### Whole-body deletion of *Acly* in adult mice results in body weight and fat loss

To investigate the essential functions of ACLY in adult animals, we generated a conditional whole-body knockout of *Acly* by tamoxifen (TAM) induction of 10- to 12-week-old *UBC-CreER*<sup>T2</sup>; *Acly*<sup>fl/fl</sup> (*Acly*<sup>Δ*UBC*</sup>) mice (Figure S1A). Body weight of both male and female *Acly*<sup>Δ*UBC*</sup> mice rapidly declined after TAM administration and remained significantly lower than that of wild-type (*Acly*<sup>fl/fl</sup>) littermates until the experimental endpoint at 5 weeks (Figure 1A). *Acly* loss was confirmed across several tissues, including liver, small intestine, brain, heart, gonadal white adipose tissue (gWAT), subcutaneous inguinal white adipose tissue (iWAT), and brown adipose tissue (BAT) (Figure S1B). Body composition analysis showed that *Acly*<sup>Δ*UBC*</sup> mice had lower fat mass than wild-type littermates, while lean mass was unchanged (Figure 1B). The reduction in fat mass was reflected by lower weight of iWAT and gWAT, which both exhibited smaller white adipocyte size (Figures 1C, 1D, and S1C). In contrast, BAT derived from *Acly*<sup>Δ*UBC*</sup> mice exhibited larger lipid vacuoles (Figures 1E and S1C), consistent with previous observations in BAT of adipocyte-specific or brown-adipocyte-specific ACLY-knockout mice.<sup>29,30</sup> The histology of other tissues examined, including liver, small intestine, and brain regions with high

expression of ACLY, the hippocampus and cerebellum,<sup>27</sup> in *Acly*<sup>Δ*UBC*</sup> mice appeared unaffected (Figure S1C).

We next assessed the metabolic implications of systemic loss of *Acly* in adult mice. No significant changes in food intake or energy expenditure were detected upon ACLY loss (Figures 1F and 1G), although during the dark cycle, there was a decrease in respiratory exchange ratio (RER) in *Acly*<sup>Δ*UBC*</sup> mice, indicating a shift in fuel use toward fats (Figure 1H). Serum non-esterified fatty acids (NEFAs) were also lower in the *Acly*<sup>Δ*UBC*</sup> mice (Figure 1I). There was no difference detected in the absorption of macronutrients, including proteins and lipids, as indicated by fecal contents of *Acly*<sup>Δ*UBC*</sup> mice (Figures 1J and 1K). Glucose tolerance was also undisturbed in *Acly*<sup>Δ*UBC*</sup> mice (Figure 1L).

Reduced movement in *Acly*<sup>Δ*UBC*</sup> mice was observed during both the light and dark cycles (Figure S1D). The rotarod assay confirmed impaired motor performance by the *Acly*<sup>Δ*UBC*</sup> mice (Figure S1E). However, hindlimb clasp reflex of *Acly*<sup>Δ*UBC*</sup> mice appeared normal (Figure S1F), indicative of intact function of spinal cord and other brain regions involved in motor responses.<sup>42</sup> In addition, Y-maze and novel object recognition tests of *Acly*<sup>Δ*UBC*</sup> mice showed no alteration in short- and long-term memory (Figures S1G and S1H). These behavioral assessments suggest that ACLY deficiency interfered with motor performance but, at least at the time points examined, did not impact basic cognitive functions. Together, these data show that *Acly* deletion results in weight and fat loss and reduced movement, but otherwise relatively mild systemic phenotypes over a 5-week period.

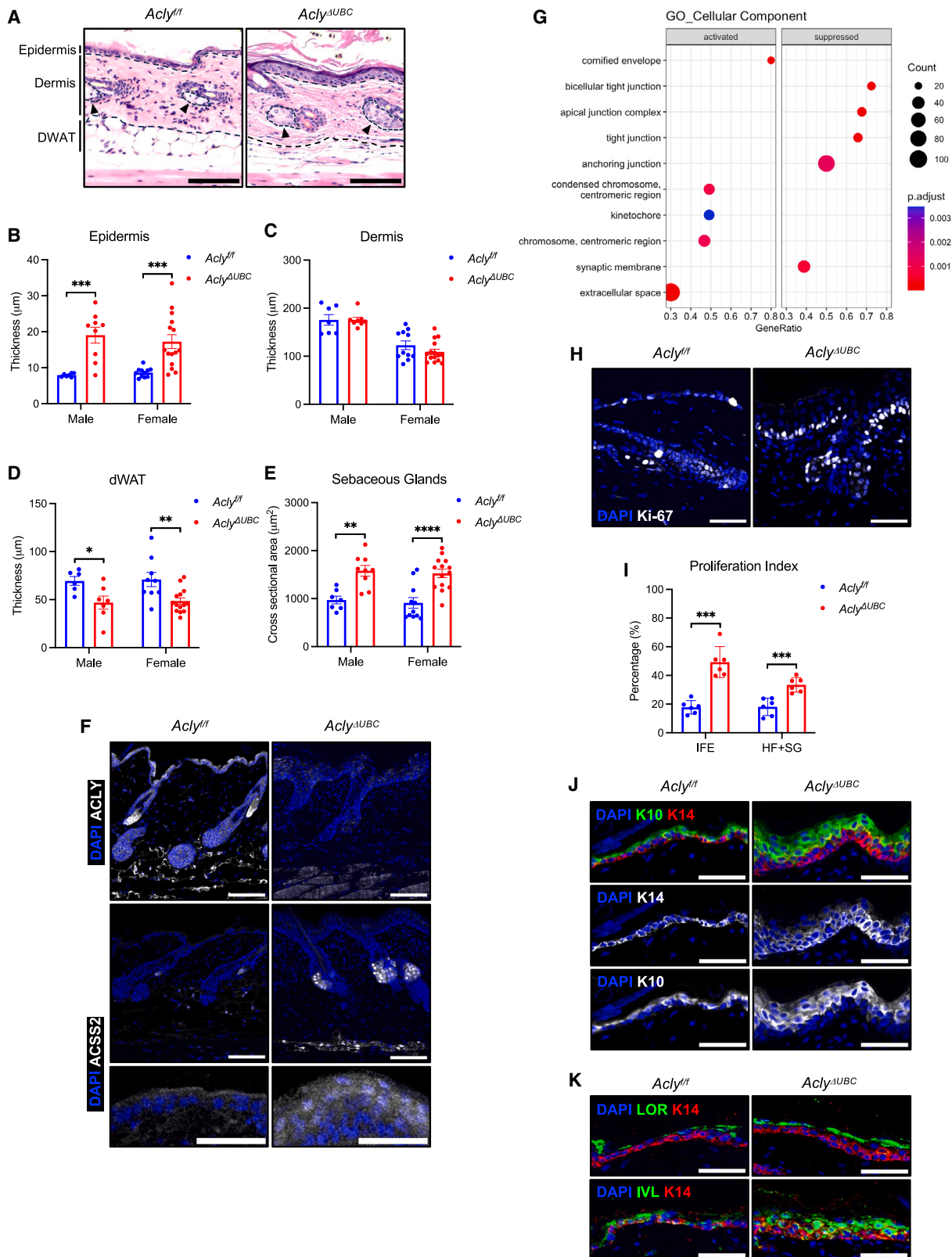
### Skin homeostasis is disrupted in whole-body *Acly* knockout mice

Although many tissues appeared grossly normal in *Acly*<sup>Δ*UBC*</sup> mice (Figure S1C), phenotypic abnormalities related to the skin and eyes were apparent. The majority of *Acly*<sup>Δ*UBC*</sup> mice started to develop dry and irritated eye conditions approximately 2 weeks after TAM induction, followed by hair graying, hair thinning, and dry and scaly skin (Figures S2A and S2B). Mammalian skin comprises three distinct layers of epidermis, dermis, and dermal white adipose tissue (dWAT), from the outside in. The epidermis continually turns over through self-renewal and differentiation of epidermal stem cells.<sup>43</sup> Hematoxylin and eosin staining of the dorsal or ventral skin from *Acly*<sup>Δ*UBC*</sup> mice revealed a thickening of the epidermis without a change in the dermis (Figures 2A–2C and S2C). The dWAT was moderately depleted, while SGs were enlarged in *Acly*<sup>Δ*UBC*</sup> mice (Figures 2A, 2D, and 2E). Immunofluorescent staining of the wild-type mouse skin showed that ACLY was highly expressed in the SGs and dWAT and less highly expressed in epidermis and hair follicles (Figure 2F), aligning with a published single-cell RNA-sequencing dataset of adult mouse skin<sup>44</sup> (Figure S2D). *Acly*<sup>Δ*UBC*</sup> skin showed efficient deletion of ACLY and robust ACSS2 upregulation, most prominently in the SGs and dWAT, although increased ACSS2 abundance could also be detected in the epidermis

(J and K) In mouse feces, (J) lipid content (males,  $n = 5$  *Acly*<sup>fl/fl</sup>,  $n = 7$  *Acly*<sup>Δ*UBC*</sup>; females,  $n = 5$  *Acly*<sup>fl/fl</sup>,  $n = 5$  *Acly*<sup>Δ*UBC*</sup>) and (K) protein content (males,  $n = 6$  *Acly*<sup>fl/fl</sup>,  $n = 6$  *Acly*<sup>Δ*UBC*</sup>; females,  $n = 4$  *Acly*<sup>fl/fl</sup>,  $n = 4$  *Acly*<sup>Δ*UBC*</sup>) were measured.

(L) Oral glucose tolerance test (GTT) (males,  $n = 4$  *Acly*<sup>fl/fl</sup>,  $n = 4$  *Acly*<sup>Δ*UBC*</sup>; females,  $n = 5$  *Acly*<sup>fl/fl</sup>,  $n = 5$  *Acly*<sup>Δ*UBC*</sup>).

Data show mean  $\pm$  SEM (A, G, H, and L) and individual mice (B–F and I–K). Statistical significance was calculated by two-way ANOVA in (A), (G), (H), and (L) and unpaired two-tailed t tests in (B–F) and (I–K) (ns, not statistically significant; \* $p \leq 0.05$ , \*\* $p \leq 0.01$ , and \*\*\* $p \leq 0.0001$ ). See also Figure S1.



(legend on next page)

(Figure 2F). Loss of ACLY and upregulation of ACSS2 were evident in *Acly*<sup>Δ<sup>UBC</sup></sup> skin by 2 weeks post TAM induction, preceding histological changes (Figures S2E–S2H). Thus, whole-body ACLY deficiency leads to increased epidermal thickness and SG size, along with ACSS2 upregulation.

Throughout the mammalian lifespan, hair follicles undergo periodic growth and regression phases that dynamically modify the skin architecture.<sup>45–47</sup> In case skin phenotypes were impacted by deletion of *Acly* during the active growth phase (anagen), when hair follicle stem cells are actively proliferating, or the active regression phase (catagen), we induced *Acly* deletion in mice at 7 weeks of age, when the hair cycle was at telogen, a resting phase.<sup>48</sup> These mice mirrored phenotypes observed upon deletion of *Acly* at 10–12 weeks of age (Figures S2I and S2J), indicating that phenotypes are independent of hair-cycle phase. For the remainder of this study, we induced gene knockout in 7-week-old mice.

To further characterize the epidermal abnormalities, we performed RNA sequencing of epidermis isolated from *Acly*<sup>Δ<sup>UBC</sup></sup> mice and wild-type littermates at 5 weeks post TAM induction and observed striking transcriptional changes (Figure S3A). Genes involved in epidermal development and differentiation and cell cycle were notably enriched in *Acly*<sup>Δ<sup>UBC</sup></sup> epidermis (Figures 2G and S3B). Consistently, Ki-67-positive cells in the interfollicular epidermis, hair follicles, and SGs also increased (Figures 2H and 2I). This pattern coincided with an increase in pan-acetylation of histones H3 and H4 (Figure S3C), a somewhat unexpected result, since ACLY deficiency reduces histone acetylation in many cell types.<sup>49</sup> Aligning with ACSS2 protein levels, *Acss2* mRNA was also increased in ACLY-deficient epidermis (Figure S3D). In the mouse epidermis, one layer of stem cells resides at the basal side, where the epidermis connects to the dermis. Basal stem cells undergo asymmetric division to self-renew and give rise to differentiated keratinocytes, which in turn migrate to the upper layers of the epidermis to replace old and damaged keratinocytes.<sup>50</sup> We postulated that the balance between self-renewal and differentiation was disturbed in *Acly*<sup>Δ<sup>UBC</sup></sup> epidermis, since most cells of the basal layer and some cells in the upper layers were positive for Ki-67 (Figure 2H). Indeed, *Acly*<sup>Δ<sup>UBC</sup></sup> epidermis showed an extensive overlap of the

basal stem cell marker keratin 14 (K14) and the differentiated keratinocyte marker keratin 10 (K10) (Figure 2J), indicative of abnormal differentiation. This result is aligned with altered Hippo and transforming growth factor β (TGF-β) signaling pathways, which control proliferation and differentiation in the epidermis (Figure S3E).<sup>51,52</sup>

Epidermal hyperplasia is a common response to injury, irritation, or inflammation, reflecting an effort to strengthen the skin barrier.<sup>53,54</sup> Although no change in immune infiltration was visually apparent (Figure S4F), many skin barrier-associated genes were elevated and tight-junction components suppressed in the epidermis of *Acly*<sup>Δ<sup>UBC</sup></sup> mice (Figures 2G and S3B). Immunofluorescent staining of the barrier proteins loricrin (LOR) and involucrin (IVL) showed increased expression along the epidermis of *Acly*<sup>Δ<sup>UBC</sup></sup> mice, further suggesting a compromised skin barrier (Figure 2K). We therefore asked if providing an artificial barrier would mitigate the skin conditions. To this end, we applied chemically inert petroleum jelly to the dorsal skin of *Acly*<sup>Δ<sup>UBC</sup></sup> mice daily over the 5-week experiment, observing reduced skin dryness and markedly improved hair regrowth (Figure S3G). Together, these data demonstrate that whole-body *Acly* deletion in adult mice results in disrupted skin homeostasis characterized by dWAT atrophy, hyperplastic epidermis and SGs, and impaired skin barrier integrity.

#### Skin-specific loss of *Acly* and *Acss2* impairs the skin barrier and induces rapid adipose tissue depletion

To determine if the cutaneous abnormalities of *Acly*<sup>Δ<sup>UBC</sup></sup> mice were driven by a skin-intrinsic effect, we first applied 4-hydroxytamoxifen (4-OHT) topically to the dorsal skin of *UBC-CreER*<sup>T2</sup>; *Acly*<sup>ff</sup> mice and observed thickened epidermis, enlarged SGs, and strong upregulation of ACSS2 in SGs (Figure 3A), concurring with the phenotypes in the *Acly*<sup>Δ<sup>UBC</sup></sup> mice. We then generated a conditional skin-specific *Acly* knockout by administering TAM to 7-week-old *KRT14-CreER*<sup>T</sup>; *Acly*<sup>ff</sup> (*Acly*<sup>Δ<sup>KRT14</sup>) mice, following the same experimental timeline as in *Acly*<sup>Δ<sup>UBC</sup></sup> mice (Figure S1A). *Acly*<sup>Δ<sup>KRT14</sup> mice recapitulated histological changes in the skin of *Acly*<sup>Δ<sup>UBC</sup></sup> mice (Figures 3B–3D), supporting the skin-intrinsic role of ACLY in maintaining tissue integrity. Unlike the whole-body knockout, loss of *Acly* in the</sup></sup>

#### Figure 2. ACLY deficiency in the adult mouse disrupts skin homeostasis

- (A) H&E staining of dorsal skin from female *Acly*<sup>ff</sup> and *Acly*<sup>Δ<sup>UBC</sup></sup> mice (scale bars, 100 μm). Dashed lines mark skin layers and outline sebaceous glands (SGs). Arrowheads point to the SGs.
  - (B–D) Thickness of dorsal skin layers, quantified in micrometers by ImageJ. Each data point is an average of three measurements from a mouse. (B) Epidermis (males,  $n = 7$  *Acly*<sup>ff</sup>,  $n = 9$  *Acly*<sup>Δ<sup>UBC</sup></sup>; females,  $n = 11$  *Acly*<sup>ff</sup>,  $n = 15$  *Acly*<sup>Δ<sup>UBC</sup></sup>), (C) dermis (males,  $n = 7$  *Acly*<sup>ff</sup>,  $n = 8$  *Acly*<sup>Δ<sup>UBC</sup></sup>; females,  $n = 11$  *Acly*<sup>ff</sup>,  $n = 15$  *Acly*<sup>Δ<sup>UBC</sup></sup>), and (D) dWAT (males,  $n = 6$  *Acly*<sup>ff</sup>,  $n = 7$  *Acly*<sup>Δ<sup>UBC</sup></sup>; females,  $n = 9$  *Acly*<sup>ff</sup>,  $n = 14$  *Acly*<sup>Δ<sup>UBC</sup></sup>).
  - (E) Areas of SG cross sections from the dorsal skin analyzed in (B) were quantified in square micrometers by ImageJ. Each data point represents the average of unique SG cross sections per H&E slide for one mouse (males,  $n = 7$  *Acly*<sup>ff</sup>,  $n = 9$  *Acly*<sup>Δ<sup>UBC</sup></sup>; females,  $n = 11$  *Acly*<sup>ff</sup>,  $n = 14$  *Acly*<sup>Δ<sup>UBC</sup></sup>).
  - (F) Immunofluorescence imaging of ACLY and ACSS2 in the dorsal skin of female *Acly*<sup>ff</sup> and *Acly*<sup>Δ<sup>UBC</sup></sup> mice (scale bars, 100 μm). To visualize ACSS2 in the epidermis (bottom), fluorescence intensity was adjusted equally in both genotypes in ImageJ (scale bars, 50 μm).
  - (G) Gene ontology (GO) enrichment analysis by clusterProfiler for the epidermis derived from whole-body *Acly* knockout (*Acly*<sup>Δ<sup>UBC</sup></sup>) compared to epidermis of wild-type mice (*Acly*<sup>ff</sup>), adjusted  $p < 0.05$ . Plot shows enriched cellular components.
  - (H) Immunofluorescent staining for Ki-67 in the dorsal skin of female *Acly*<sup>ff</sup> and *Acly*<sup>Δ<sup>UBC</sup></sup> mice (scale bars, 50 μm).
  - (I) Proliferation indices, calculated from the percentage of cells that were positive for Ki-67 in the interfollicular epidermis (IFE), hair follicle (HF), and SGs. Data show biological replicates (*Acly*<sup>ff</sup>,  $n = 6$ ; *Acly*<sup>Δ<sup>UBC</sup></sup>,  $n = 6$ ).
  - (J and K) Immunofluorescent staining for (J) keratin 10 (K10) and keratin 14 (K14) and (K) loricrin (LOR) and involucrin (IVL) in the dorsal skin of female *Acly*<sup>ff</sup> and *Acly*<sup>Δ<sup>UBC</sup></sup> mice (scale bars, 50 μm).
- Data show individual mice (B–E and I). Statistical significance was calculated by unpaired two-tailed t tests in (B–E) and (I) (ns, not statistically significant; \* $p \leq 0.05$ , \*\* $p \leq 0.01$ , \*\*\* $p \leq 0.001$ , and \*\*\*\* $p \leq 0.0001$ ). See also Figures S2 and S3.

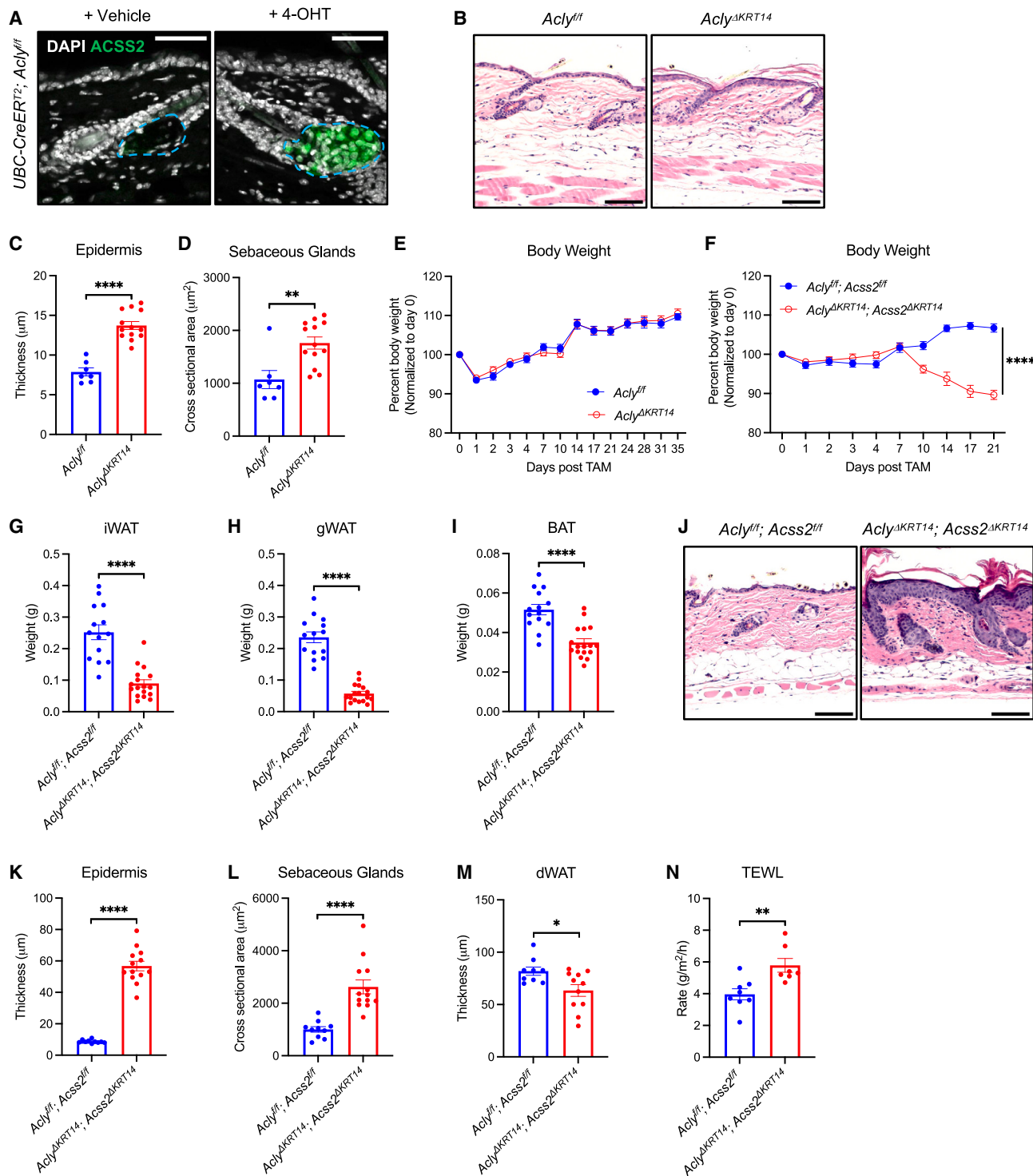


**Figure 3. Skin-specific deletion of ACLY and ACSS2 impairs skin barrier function and induces rapid fat loss**

(A) Immunofluorescence imaging of ACSS2 in the dorsal skin of female *UBC-CreER<sup>T2</sup>; Acly<sup>+/+</sup>* mice 5 weeks after topical application of ethanol (vehicle) or 4-hydroxytamoxifen (4-OHT) (+vehicle,  $n = 2$ ; +4-OHT,  $n = 4$ ). Blue dashed outlines show SGs (scale bars, 50  $\mu\text{m}$ ).

(B) H&E staining of dorsal skin of female wild-type (*Acly<sup>+/+</sup>*) and skin-specific *Acly*-knockout (*Acly<sup>ΔKRT14</sup>*) mice (scale bars, 100  $\mu\text{m}$ ).

(C) Thickness of epidermis in the dorsal skin was quantified in micrometers by ImageJ. Each data point is an average of three measurements from a mouse (*Acly<sup>+/+</sup>*,  $n = 7$ ; *Acly<sup>ΔKRT14</sup>*,  $n = 13$ ).

(legend continued on next page)

skin did not induce weight loss (Figure 3E), indicating contributions of other cell types to the weight loss phenotype. Since adipose tissues of *Acly*<sup>Δ<sup>ABC</sup> mice were strongly affected, we asked if dual loss of *Acly* from adipocytes and skin would resemble the severity of skin and/or weight-loss phenotypes in *Acly*<sup>Δ<sup>ABC</sup> mice. However, *Acly* deletion from both skin and adipose tissue (*Acly*<sup>Δ<sup>KRT14</sup>; *ΔADIPQ*) did not exacerbate these phenotypes compared to those in *Acly*<sup>Δ<sup>KRT14</sup> mice (Figures S4A–S4C). Thus, epidermal thickening and SG enlargement phenotypes are driven by *Acly* loss in the skin.</sup></sup></sup></sup>

Since ACSS2 was robustly upregulated across skin compartments upon ACLY loss (Figure 2F), we hypothesized that it may play a partial compensatory role in the absence of ACLY. We first examined skin-specific *Acss2*-knockout (*Acss2*<sup>Δ<sup>KRT14</sup>) mice, finding no obvious changes in skin histology (Figures S4D and S4E). To test the requirement of ACSS2 in the skin upon ACLY loss, we generated an inducible DKO of *Acly* and *Acss2* in the mouse skin (*Acly*<sup>Δ<sup>KRT14</sup>, *Acss2*<sup>Δ<sup>KRT14</sup>) (Figure S4F). Strikingly, deletion of both *Acly* and *Acss2* in the skin triggered rapid weight loss that prompted an early termination of the experiments by 3 weeks post TAM induction (Figure 3F). DKO mice showed a drastic depletion of adipose tissues (Figures 3G–3I), with no change in liver weight or histology (Figures S4G and S4H). Although the tongue expresses some level of K14, the tissue architecture of tongue in DKO mice appeared normal (Figure S4H). These mice displayed more severe external morphologies than single ACLY knockouts with 100% penetrance for both eye irritation and hair loss (Figures S4I and S4J). Hyperplasia in the epidermis and the SGs was dramatically exacerbated, and accordingly, proliferation indices were elevated (Figures 3J–3L, S4K, and S4L). No obvious changes in pan-acetylation of histone H3 and H4 were detected in DKO skin (Figure S4M). The dWAT layer was depleted to a level comparable to that of *Acly*<sup>Δ<sup>ABC</sup> dWAT (Figure 3M). To quantitatively test the functional properties of the skin barrier in these mice, we measured transepidermal water loss (TEWL), finding that it was significantly elevated in DKO over wild-type littermates, confirming reduced skin barrier function (Figure 3N). These findings corroborate that nucleocytosolic acetyl-CoA production within the skin is crucial for maintaining barrier function and tissue homeostasis and further show that loss of key skin acetyl-CoA-producing enzymes promotes rapid loss of body fat.</sup></sup></sup></sup>

### Deficient nucleocytosolic acetyl-CoA synthesis in the skin triggers dependence on exogenous lipids

Since acetyl-CoA is necessary for fatty acid synthesis, we hypothesized that loss of ACLY and ACSS2 in the skin might increase demand for exogenous fatty acids in the skin and that adipose lipolysis might increase in these animals, releasing fatty acids.<sup>55</sup> In support of this notion, hormone-sensitive lipase (HSL) phosphorylation (S563) increased in gWAT of DKO mice (Figure 4A). Concordantly, we also observed increased gene expression of HSL (encoded by *Lipe*) and adipose triglyceride lipase (ATGL; encoded by *Pnpla2*) in BAT (Figure S5A). These observations coincided with elevated serum levels of NEFAs but not with other lipid classes that were examined by thin-layer chromatography (TLC) (Figures 4B and S5B). We predicted that skin and systemic phenotypes in DKO mice might be mitigated by increasing dietary lipids. Indeed, olive oil supplementation by oral gavage increased body weight in DKO mice (Figure 4C), blocked the increase in level of circulating NEFAs (Figure 4D), suppressed overexpression of lipolysis genes in BAT (Figure S5A), decreased p-HSL-S563 in gWAT (Figure 4E), and augmented lipid droplet size in both gWAT and BAT (Figure 4F). In addition, olive oil supplementation improved skin histological abnormalities (Figures 4G and 4H).

We also considered the possibility that weight loss in DKO mice might also be partially explained by activation of non-shivering thermogenesis in adipose tissues in response to heat loss due to impaired skin barrier function. Prior studies have shown that disrupting specific lipid metabolism genes (e.g., *Scd1* and *Vdr*) in the skin activates thermogenesis and renders the mice resistant to diet-induced obesity.<sup>56,57</sup> In the BAT of male but not female DKO mice, we detected higher expression of uncoupling protein 1 (*Ucp1*), as well as creatine kinase B (*Ckb*) and glycine amidino transferase (*Gatm*), genes associated with the futile creatine cycle, a UCP1-independent thermogenic program<sup>58</sup> (Figure S5C), and these genes were partially suppressed by olive oil supplementation (Figure S5D). In line with this, male but not female DKO mice exhibited higher energy expenditure than wild-type littermates during the light cycle (Figure S5E). Despite the differences in thermogenic activation, weight loss and increased p-HSL and gene expression of lipolytic enzymes were comparable between sexes (Figures 4A, S5C, and S5F). Moreover, circulating free fatty acids were elevated in both male and female mice (Figure S5B), consistent with an induction

(D) Areas of sebaceous gland cross sections from the dorsal skin analyzed in (C) were quantified in square micrometers by ImageJ. Each data point represents the average of unique SG cross sections per H&E slide for one mouse.

(E) Body weight of wild-type (*Acly*<sup>ff</sup>) and skin-specific *Acly*-knockout (*Acly*<sup>Δ<sup>KRT14</sup>) mice over 5 weeks post tamoxifen (TAM) induction. Each time point is normalized to day 0 (*Acly*<sup>ff</sup>, *n* = 12; *Acly*<sup>Δ<sup>KRT14</sup>, *n* = 16).</sup></sup>

(F) Body weight of wild-type (*Acly*<sup>ff</sup>; *Acss2*<sup>ff</sup>) and skin-specific double-knockout (DKO) of *Acly* and *Acss2* (*Acly*<sup>Δ<sup>KRT14</sup>; *Acss2*<sup>Δ<sup>KRT14</sup>) mice over 3 weeks (wild type, *n* = 12; DKO, *n* = 16).</sup></sup>

(G–I) Weight of adipose tissues in wild-type (*n* = 14) and DKO mice (*n* = 17). (G) iWAT, (H) gWAT, and (I) BAT.

(J) H&E staining of dorsal skin from male wild-type and DKO mice (scale bars, 100 μm).

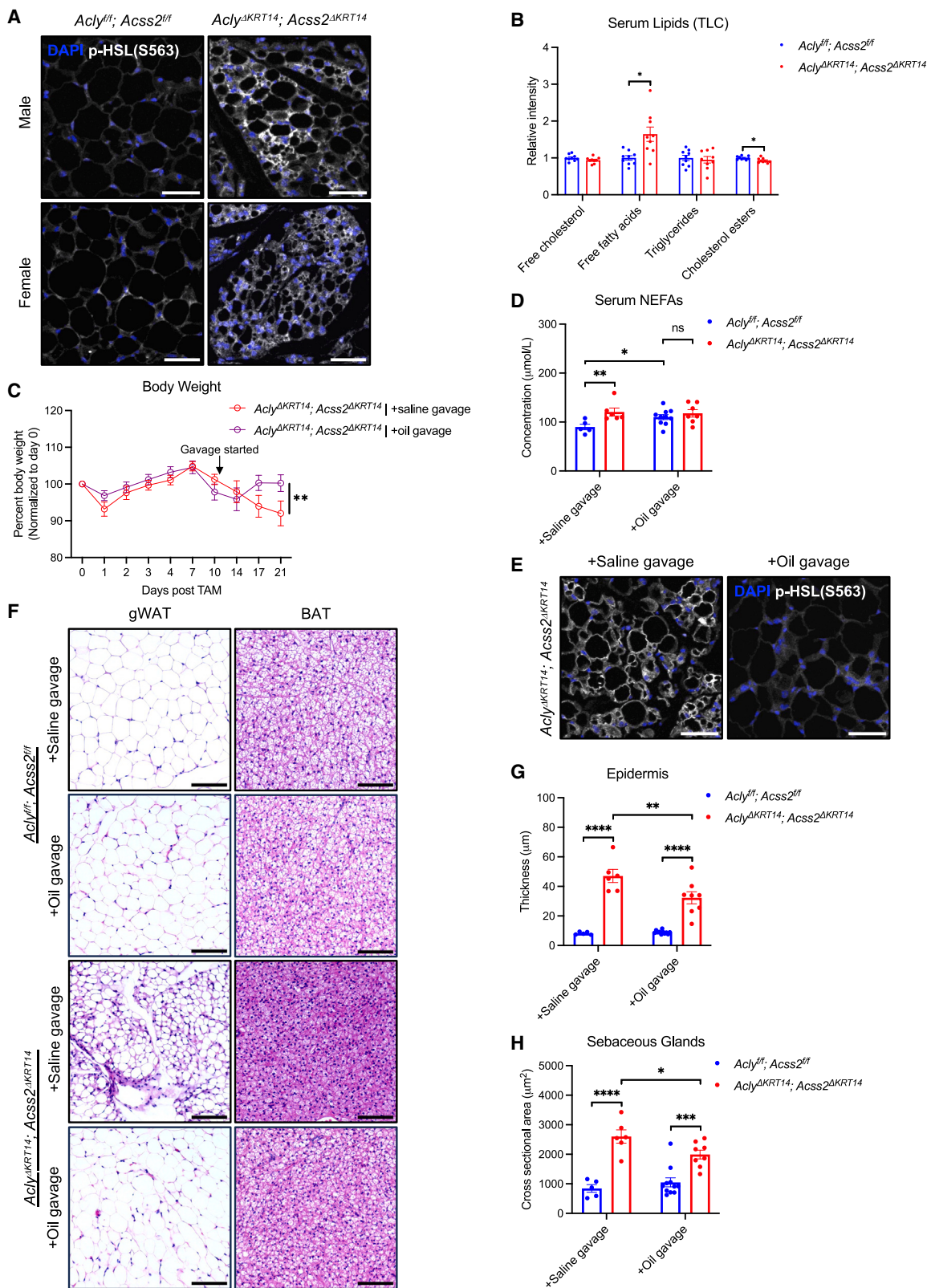
(K) Thickness of epidermis in dorsal skin (wild type, *n* = 10; DKO, *n* = 13).

(L) Areas of SG cross sections from dorsal skin analyzed in (K).

(M) Thickness of dWAT in dorsal skin (wild type, *n* = 9; DKO, *n* = 11).

(N) Transepidermal water loss (TEWL) was measured (wild type, *n* = 8; DKO, *n* = 7). Each data point is an average of 30 1-s readings from each mouse.

Data show mean ± SEM (E and F) and individual mice (C, D, G–I, and K–N). Statistical significance was calculated by two-way ANOVA in (E) and (F) and unpaired two-sided t tests in (C), (D), (G–I), and (K–N) (ns, not statistically significant; \**p* ≤ 0.05, \*\**p* ≤ 0.01, and \*\*\**p* ≤ 0.0001). See also Figure S4.



(legend on next page)

of adipose lipolysis in both sexes. Therefore, enhanced thermogenesis may be one mechanism contributing to fat loss and weight loss in DKO mice, particularly in males, but may not account for the full effect.

To further test the relationship between dietary fat, skin acetyl-CoA synthesis, body weight, and skin phenotypes, we sought to limit dietary fat. For this we used the *Acly*<sup>-/-</sup>*KRT14*<sup>-/-</sup> mice, since the phenotype of the DKO mice was already severe. Indeed, *Acly*<sup>-/-</sup>*KRT14*<sup>-/-</sup> mice fed a zero-fat diet (ZFD) lost weight and showed exacerbated epidermal and sebaceous hyperplasia (Figures S5G–S5I). Finally, to test the interplay between skin ACLY and exogenous lipids in a tractable human system, we treated primary human keratinocytes with the ACLY inhibitor BMS-303141. As expected, cultured human keratinocytes showed robust ACSS2 upregulation upon ACLY inhibition, accompanied by diminished expression of *MKI67* and *KRT14* and reduced cell proliferation (Figures S5J and S5K). Supplementation of exogenous fatty acids (palmitic acid and oleic acid) reversed these effects (Figures S5J and S5K). Although the *in vitro* effect of ACLY inhibition on proliferation is distinct from that seen *in vivo* with ACLY deficiency within a complex tissue environment, the data indicate that human keratinocytes are responsive to acetyl-CoA availability in a fatty acid-dependent manner. Together, these results demonstrate that disruption of acetyl-CoA synthesis renders the skin highly sensitive to the availability of exogenous lipids.

#### ACLY and ACSS2 are required for maintaining lipid composition in the epidermis

We surmised that impaired skin barrier function in mice lacking acetyl-CoA-synthesizing enzymes might be a result of disturbed skin lipid content, and that might be rescued by increasing exogenous lipids. Oil red O staining revealed a loss of neutral lipids in the epidermis of DKO mice, while staining intensity in SGs was comparable between genotypes (Figure 5A). However, despite providing partial rescue of both the skin and the systemic phenotypes, olive oil supplementation did not restore the level of neutral lipids in the DKO epidermis (Figure 5A), prompting us to investigate the changes in epidermal lipid profile more deeply.

We first surveyed broad lipid classes in the DKO epidermis by TLC and found a pronounced depletion of triglycerides, which

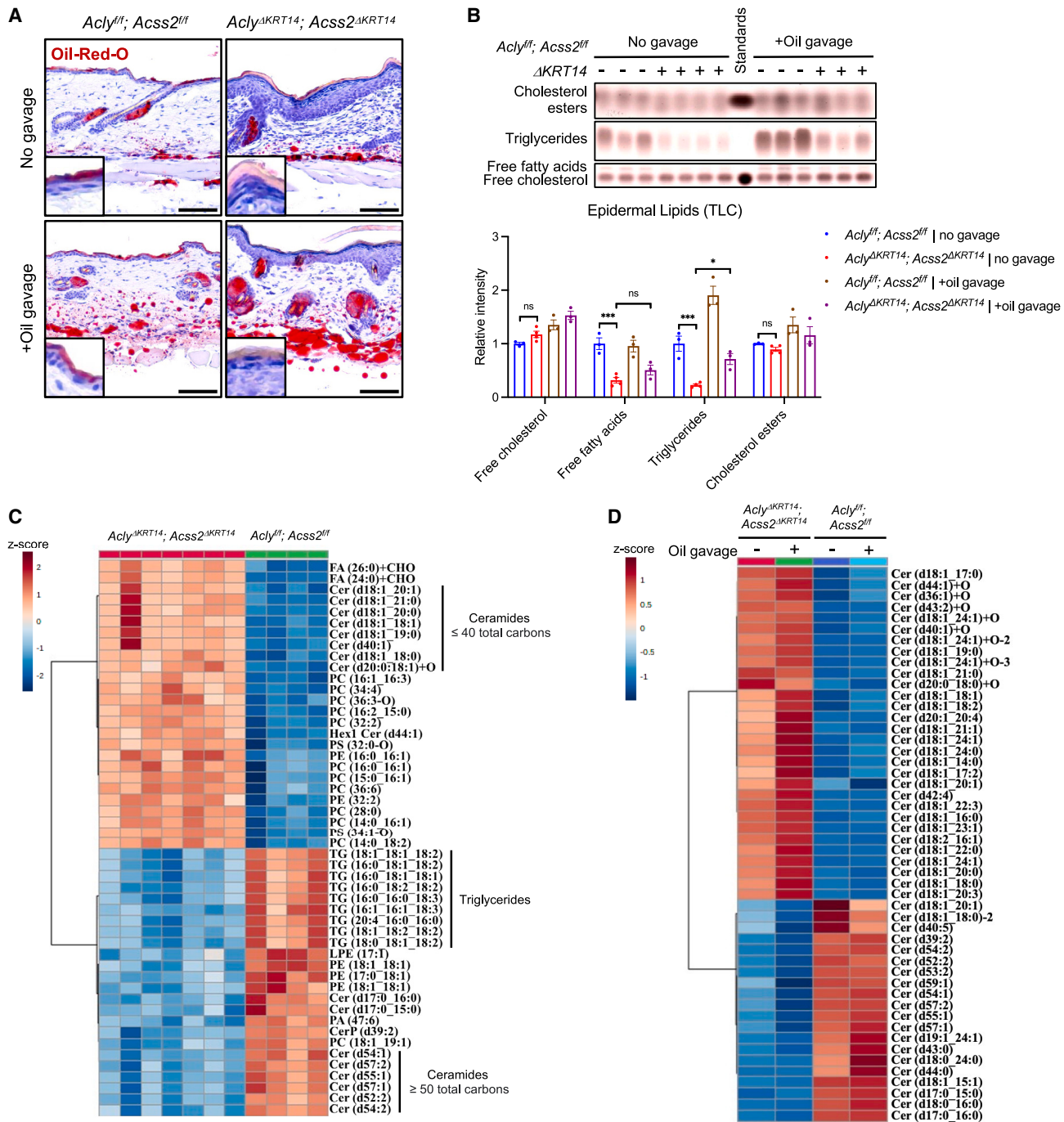
was modestly restored by olive oil supplementation (Figure 5B). Epidermal free cholesterol and cholesterol esters were unchanged in DKO mice, while free fatty acids were reduced (Figure 5B). A comprehensive analysis of individual lipid species by lipidomics confirmed a global reduction of triglycerides and altered composition of ceramides in DKO epidermis (Figure 5C and Table S1). Specifically, we observed a reduction in ceramides containing very long fatty acyl chains, particularly ceramides containing greater than 50 total carbons, summing the 18-carbon sphingosine backbone and the acyl chain (Figure 5C and Table S1). In contrast, ceramides with somewhat shorter fatty acyl chains (40 or fewer total carbons in the ceramide molecule) accumulated in the DKO mouse epidermis (Figure 5C and Table S1). The reduced acyl chain length in DKO mice is noteworthy, since ceramides containing highly elongated fatty acyl chains are hallmarks of the mammalian skin barrier.<sup>59</sup> However, these patterns were unchanged by olive oil supplementation (Figure 5D). Since acetyl-CoA is required for fatty acid elongation,<sup>59,60</sup> this disturbed balance of ceramide composition is consistent with deficient cytosolic acetyl-CoA in the DKO epidermis that is not rescued by exogenous fatty acids. Therefore, the data indicate that ACLY and ACSS2 in the skin are necessary for proper epidermal production of lipids that comprise the skin barrier.

#### Sebum production increases in ACLY- and ACSS2-deficient skin

Aside from the epidermis, SGs are the other major lipid-producing compartment in the skin, and as noted, we observed undisturbed neutral lipid staining in the DKO SGs (Figure 5A). This was intriguing, since SGs are considered a major site of *de novo* lipogenesis (DNL),<sup>61</sup> and ACSS2 is dramatically upregulated there in the absence of ACLY. Hence, we speculated that additional compensatory mechanisms, such as lipid uptake, account for sustained sebum production in this model. First, we surveyed broad lipid classes in the sebum of DKO mice, finding minimal changes between genotypes, although a modest increase in wax esters, which are sebum-specific lipids, was observed (Figure 6A). Moreover, in contrast to the drastic reduction in triglycerides from epidermis, triglycerides were not depleted from the sebum (Figure 6B), and the total amount of sebum produced

**Figure 4. Double knockout of *Acly* and *Acss2* in the skin triggers adipose lipolysis in a diet-dependent manner**

- (A) Immunofluorescence imaging of p-HSL (S563) in the gonadal white adipose tissue (gWAT) of wild-type (*Acly*<sup>+/+</sup>; *Acss2*<sup>+/+</sup>) and DKO (*Acly*<sup>-/-</sup>, *Acss2*<sup>-/-</sup>) mice fed *ad libitum* (scale bars, 50 μm).
  - (B) Serum lipids from wild-type and skin-specific DKO mice fed *ad libitum* were separated by thin-layer chromatography (TLC) (males, *n* = 3 wild type, *n* = 4 DKO; females, *n* = 6 wild type, *n* = 5 DKO). Band intensity of lipid classes was quantified by ImageJ and normalized to the serum lipids of wild-type mice.
  - (C) Body weight of DKO mice gavaged with saline (+saline gavage) versus olive oil (+oil gavage) (gavages given every other day starting on day 11, indicated by arrow). Each time point is normalized to day 0 (DKO + saline, *n* = 7; DKO + oil, *n* = 12).
  - (D) Serum non-esterified fatty acids (NEFAs) (μmol/L) in wild-type and DKO mice with saline versus oil gavage and fed *ad libitum* were measured by colorimetric assay (wild type + saline, *n* = 5; DKO + saline, *n* = 6; wild type + oil, *n* = 10; DKO + oil, *n* = 7).
  - (E) Immunofluorescence imaging of p-HSL (S563) in gWAT of male DKO mice fed *ad libitum*, with saline versus oil gavage (scale bars, 50 μm).
  - (F) H&E staining of gWAT and BAT in male wild-type and DKO mice with saline versus oil gavage (scale bars, 100 μm).
  - (G) Thickness of epidermis in the dorsal skin was quantified in micrometers by ImageJ. Each data point is an average of three measurements from a mouse (wild type + saline, *n* = 5; DKO + saline, *n* = 6; wild type + oil, *n* = 11; DKO + oil, *n* = 8).
  - (H) Areas of sebaceous gland cross sections from the dorsal skin in (F) were quantified in square micrometers by ImageJ. Each data point represents the average of unique SG cross sections per H&E slide for one mouse.
- Data show mean ± SEM (C) and individual mice (B, D, G, and H). Statistical significance was calculated by two-way ANOVA in (C), (D), (G), and (H) and unpaired two-sided t tests in (B) (ns, not statistically significant; \**p* ≤ 0.05, \*\**p* ≤ 0.01, \*\*\**p* ≤ 0.001, and \*\*\*\**p* ≤ 0.0001). See also Figure S5.



(legend continued on next page)

was modestly enhanced in DKO mice (Figure 6C). Intriguingly, olive oil gavage, which mitigated adipose lipolysis in DKO mice (Figures 4E and S5A), further enhanced the sebum overproduction phenotype (Figure 6C). These data suggest that SGs might be an important destination for circulating lipids when ACLY and ACSS2 are deficient. Consistent with this notion, we noted that protein expression of the fatty acid transporter CD36 increased in both epidermis and SGs of DKO mice and was further amplified with olive oil treatment (Figure 6D). Olive oil supplementation also augmented CD36 abundance in SGs of wild-type mice (Figure 6D), indicating responsivity to changes in exogenous lipid availability even in ACLY-proficient animals. Since, in contrast to the DKO mice, whole-body *Acly*-knockout mice had lower serum NEFAs (Figure 1I), we also measured sebum production in this model. Indeed, we found that *Acly*<sup>ΔUBC</sup> mice produced less sebum than wild-type littermates (Figure 6E), highlighting distinct phenotypes in the whole body versus skin-specific knockout models as well as the relationship between circulating fatty acids and sebum production when skin acetyl-CoA production is impaired.

We set out to further understand how circulating lipids support sebum production in DKO mice by examining the composition of sebum lipids and comparing it to that in serum. We quantified the relative abundance of saponified fatty acids between genotypes in both serum and sebum, observing increased abundance of most fatty acids detected (ranging from C14:0 to C26:0) in the sebum of DKO mice, mirroring the trends observed in the serum (Figures 6F and 6G), but not in the epidermis (Figure 6H). Of note, this analysis did not capture the most highly elongated fatty acids that were the most strikingly suppressed in the epidermal ceramide pool in the lipidomics analysis. Notably, linoleic acid (C18:2), a diet-derived essential fatty acid with roles in skin barrier function,<sup>62</sup> was enriched in the sebum of DKO versus wild-type mice, further supporting the notion that circulating lipids are taken up by SGs to support sebum production. Together, these data suggest that sebum production is promoted in the absence of ACLY and ACSS2 through uptake of circulating fatty acids, likely leveraging fatty acids derived from both diet and adipose lipolysis.

#### Transcriptional profiles of skin lacking both ACLY and ACSS2 reveal changes in inflammatory responses, lipid metabolism, and secreted factors

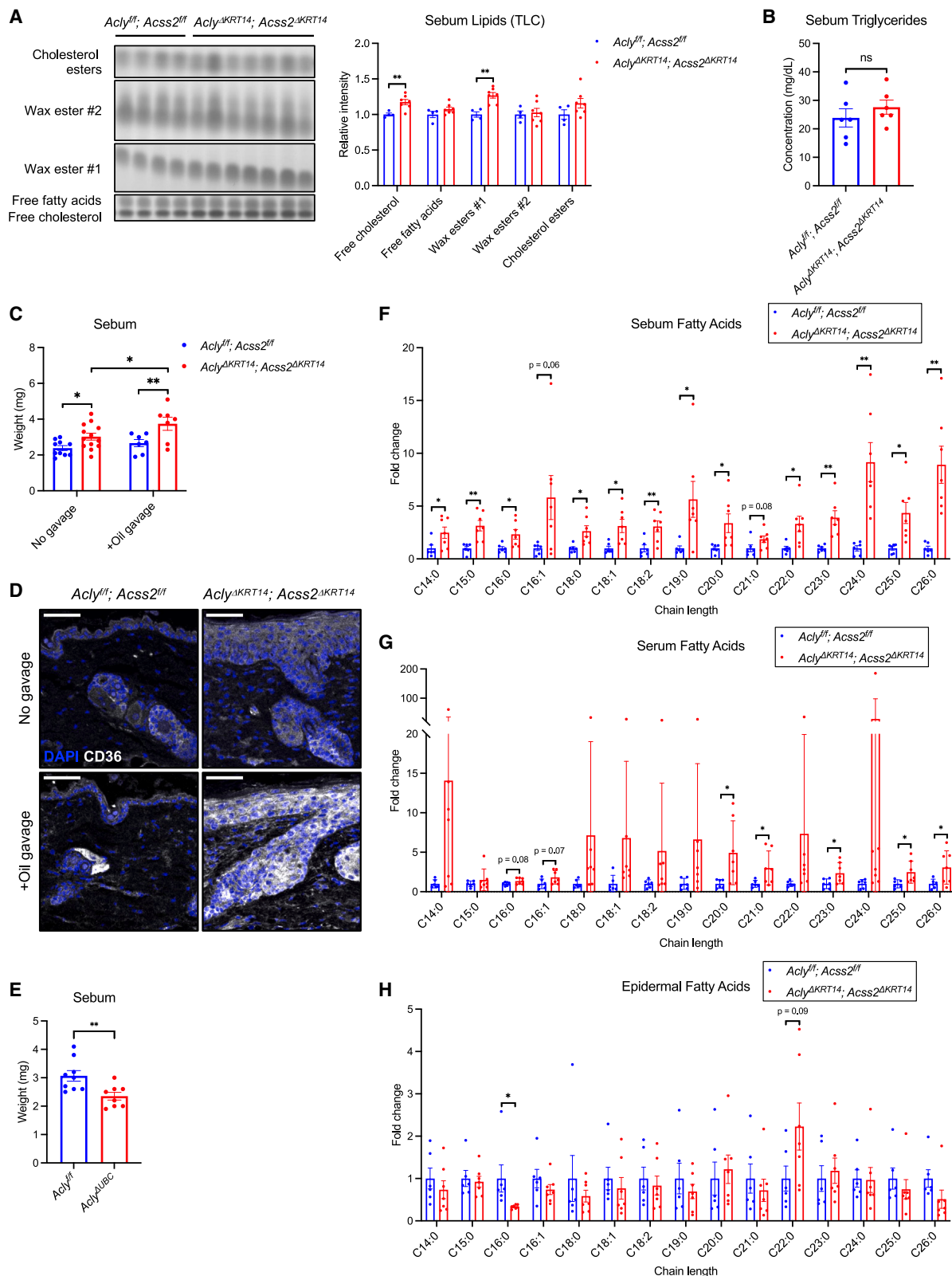
To gain mechanistic insight into factors that might link skin to systemic phenotypes in DKO mice, we carried out RNA sequencing of epidermis at two time points, day 12 and day 21 post TAM induction. At day 12, fat loss was apparent and adipose lipolysis was activated, but skin phenotypes had not yet emerged (Figures S6A–S6F). However, gene expression of epidermal proliferation and differentiation markers was already altered (Figure S6G). We examined transcriptional changes at

this early time point to increase the likelihood of capturing primary effects of perturbed acetyl-CoA metabolism versus secondary effects of severely disrupted skin homeostasis. At day 12, we observed relatively modest differential gene expression changes with an enrichment of inflammatory and proliferative signatures (Figures 7A, S6H, and S6I). By day 21, lipid metabolism gene expression signatures became prominent, along with inflammatory processes and proliferation (Figures 7B, S6J, and S6K).

We hypothesized that factors regulating the local and systemic phenotypes in this mouse model are likely secreted factors. Thus, we curated a list of genes encoding secreted proteins from the UniProt database (Table S2) and overlapped it with epidermal genes that were significantly upregulated at both day 12 and day 21, finding 62 genes meeting these criteria (Figure 7C and Table S3). The majority of genes encoding secreted proteins showed progressive upregulation from day 12 to day 21 (Figure 7D). One significantly upregulated gene was *Tslp*, which encodes an epidermal cytokine that promotes sebum secretion and adipose lipolysis when overexpressed systemically and, to our knowledge, is the only factor that has been demonstrated to link these two processes.<sup>63</sup> TSLP expression is concentrated within SG-rich skin and correlates with the expression of genes involved in sebum production.<sup>63,64</sup> In DKO mice, we detected a marked increase in the level of TSLP in the serum (Figure S7A), nominating it as a plausible factor linking these phenotypes in our mouse model. The effects of TSLP on sebum hyperproduction and fat loss have been shown to be dependent on T cells, since depletion of T cells abolished these TSLP-driven phenotypes.<sup>63</sup> Aligning with the immune-related gene expression profile at day 12, we observed increased abundance of CD3<sup>+</sup> T cells in DKO skin at this time point (Figure S7B). We therefore asked if depleting T cells would alleviate skin and adipose phenotypes in the DKO mouse model (Figures S7C–S7E). However, in this model, loss of T cells did not alter body weight or fat loss, epidermal thickness, SG size, or sebum production (Figures S7F–S7J), suggesting that TSLP is unlikely to be a sole driver for these effects in this model, at least through its effects on T cells, and the phenotype is likely more complex than can be accounted for by a single factor.

To understand if lipid supplementation impacts gene expression in the DKO epidermis in conjunction with improved systemic adiposity, we selected several top upregulated genes encoding secreted proteins that have been linked to adipose tissue lipid metabolism in previous studies (Table S3), finding that many were regulated by olive oil supplementation, with most showing decreased expression, while others either increased or remained unchanged (Figure 7E). These observations indicate that the skin is highly responsive to acetyl-CoA deprivation and lipid availability.

(D) Hierarchical clustering heatmap of the top 50 most differentially expressed ceramides in the epidermis of wild-type and DKO mice and in combination with olive oil supplementation (wild type,  $n = 4$ ; DKO,  $n = 7$ ; wild type + oil gavage,  $n = 7$ ; DKO + oil gavage,  $n = 6$ ). For (C) and (D), data were log10 transformed and auto-scaled in each heatmap with hierarchical clustering by Euclidean distance with the Ward clustering algorithm. A conservative non-parametric t test assuming unequal variance due to the limited sample size was used for the two-group analysis (C) and one-way ANOVA for the four-group comparison (D). Statistical significance was calculated by two-way ANOVA in (B) (ns, not statistically significant; \* $p \leq 0.05$ , \*\* $p \leq 0.01$ , \*\*\* $p \leq 0.001$ , and \*\*\*\* $p \leq 0.0001$ ). See also Table S1.



(legend on next page)

Altogether, the data align with a model in which acetyl-CoA limitation in the skin disrupts epidermal barrier lipids and triggers multifaceted compensatory responses to mitigate barrier disruption, including promoting sebum production, likely through increased use of circulating lipids (Figure 7F). Our data highlight the distinct effects of acetyl-CoA limitation on lipid profiles of epidermis versus SGs and reveal interplay between skin and adipose tissues, thus establishing a role for skin acetyl-CoA synthesis in the maintenance of systemic lipid homeostasis.

## DISCUSSION

The skin protects the body from the external environment by preventing water loss, heat loss, mechanical insults, microbial invasion, and entry of xenobiotics and UV radiation.<sup>65</sup> Lipids are essential components of the skin barrier.<sup>66</sup> In the DKO mouse model, we observe a perturbed ceramide pool in a manner consistent with defective fatty acid elongation. Ceramides are synthesized from 18-carbon sphingosine and a fatty acid of varying chain length joined by an amide bond. Ceramides produced from very-long-chain fatty acids are highly enriched in the skin, where they contribute to the structural properties of the skin barrier.<sup>67</sup> Our findings align with prior studies that have shown that deficiency of enzymes for fatty acid elongation or synthesis of ceramides containing very long acyl chains results in skin barrier dysfunction.<sup>68–72</sup> Importantly, mutations of these genes have been linked to both hereditary and sporadic cases of skin disorders such as ichthyoses, psoriasis, and atopic dermatitis.<sup>67</sup> Beyond elongation, the fatty acid synthase inhibitor TVB-2640 is being tested in clinical trials against several cancers, and dry skin conditions have been reported.<sup>73</sup> Thus, the current data build on substantial prior literature demonstrating the importance of fatty acid metabolism in maintaining the skin barrier. Moreover, a number of prior studies manipulating skin lipid metabolism (e.g., *Scd1*,<sup>56</sup> *Acbp*,<sup>74–76</sup> *Elov3*,<sup>77</sup> and *Dgat1*<sup>78</sup>) have reported systemic metabolic phenotypes, including impaired thermoregulation, increased energy expenditure, and resistance to diet-induced obesity. In addition, a recent study that administered radiolabeled triglycerides to mice found that the skin is a major destination of dietary fat.<sup>79</sup> Although the skin's role in metabolic physiology is often overlooked, our findings substantiate the growing recognition that skin is a critical participant in regulating systemic lipid metabolism.

Despite strong expression of ACLY and ACSS2 in the SGs, sebum is surprisingly elevated in DKO mice. This observation

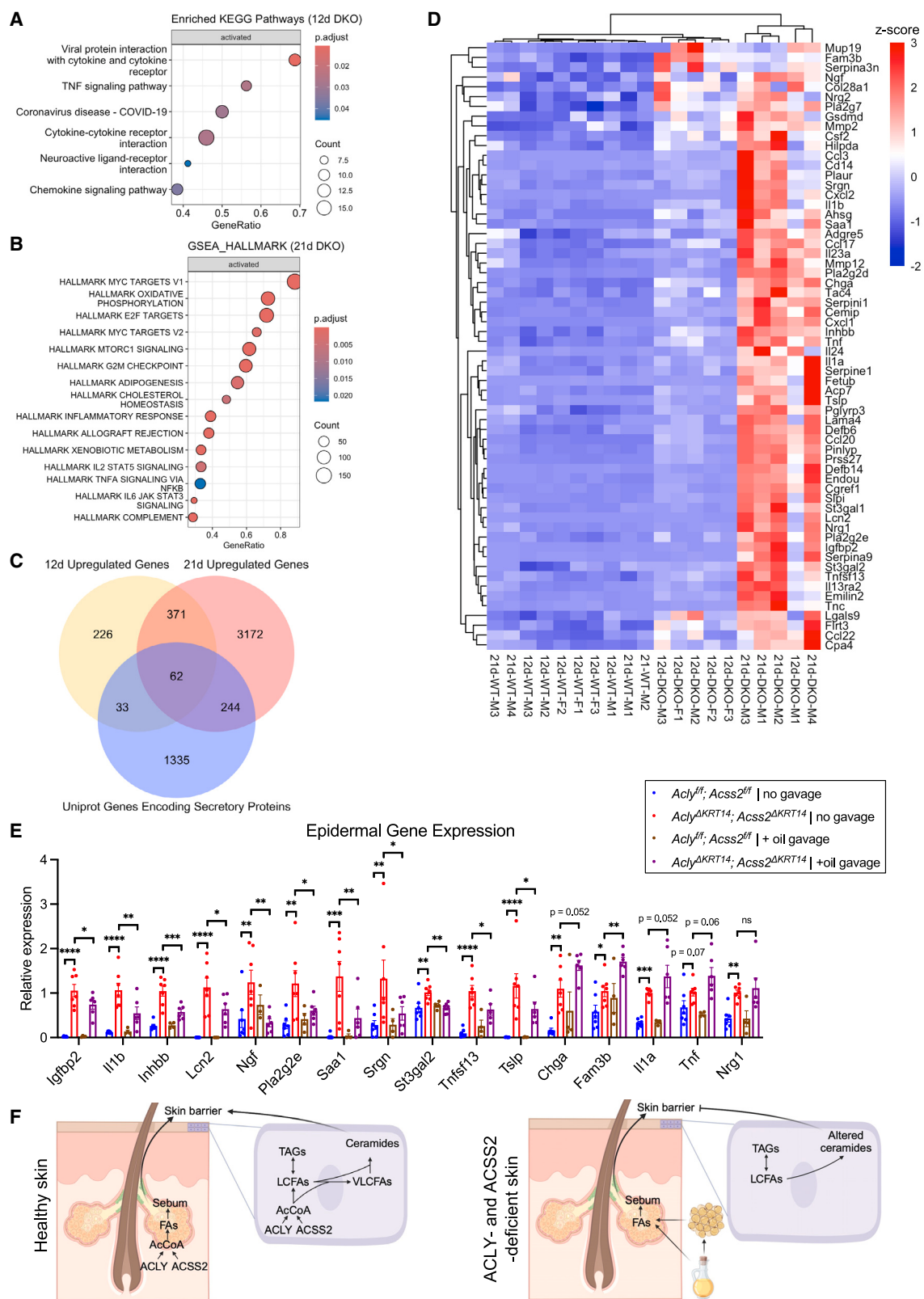
raised the questions of how sebum production is augmented, what signaling cues drive this response, and what alternative sources of fatty acids feed sebaceous lipid production. Although previous work has demonstrated that the cytokine TSLP activates T cells to drive sebum production, and that overexpression of TSLP could trigger adipose depletion to support sebum hypersecretion,<sup>63</sup> and we observe potent upregulation of TSLP in the DKO mice, T cell depletion does not impact the phenotypes in this model, suggesting that it likely is not the sole factor driving the sebum production and fat loss phenotypes in this model. Transcriptional profiles of DKO mice exhibit massive changes in genes encoding cytokines and other secreted factors and lipid metabolism proteins that are responsive to dietary lipid availability, pointing to a complex response to acetyl-CoA deficiency. Interestingly, several secreted proteins encoded by genes that are identified in our DKO mouse epidermis, including *Ahsg*, *Ccl20*, *Cd14*, *Fetub*, *Igfbp2*, *Lgals9*, *Saa1*, and *Tnfsf13*, are differentially expressed in the plasma of human subjects undergoing intermittent fasting, acute caloric restriction, and prolonged weight loss.<sup>80–83</sup> Another outstanding question is how exogenous lipid supplementation differentially impacts the SGs versus epidermis when acetyl-CoA is limited. Although the perturbed ceramide pool was not rescued, we observed CD36 upregulation within the epidermis of DKO skin, and lipid supplementation rescued effects of ACLY inhibition in cultured keratinocytes. This raises the possibility that specific lipid species or lipid-derived signals within the epidermis may directly contribute to improving the skin barrier in this model, warranting further investigation.

Aside from an increase in skin's demand for lipids, we found that BAT thermogenesis might in part account for fat loss in DKO mice; however, only male animals displayed both transcriptional activation of thermogenic genes and increased energy expenditure. Sexual dimorphism in terms of thermogenic activation in BAT can be influenced by various factors, such as cold temperature, diet, and age.<sup>84</sup> Furthermore, it is unclear if activation of thermogenic genes in the BAT of DKO mice was a direct response to heat loss or a secondary effect of excessive lipolysis, because chemically induced lipolysis can trigger transcriptional upregulation of thermogenic genes in mouse BAT in the absence of thermoregulatory demand.<sup>85</sup> Regardless, the similar skin and systemic phenotypes observed in male and female DKO mice suggest that thermogenesis activation is unlikely to be the only factor driving fat loss in this model.

Although adipose tissues were strongly affected in whole-body Acly-knockout mice, we showed that ACLY-deficient

**Figure 6. Sebum production unexpectedly increases in ACLY- and ACSS2-deficient skin**

- (A) Sebum lipids from wild-type (*Acly*<sup>+/+</sup>, *Acss2*<sup>+/+</sup>) and DKO (*Acly*<sup>-/-KRT14</sup>, *Acss2*<sup>-/-KRT14</sup>) mice separated by thin-layer chromatography (TLC) (wild type, *n* = 4; DKO, *n* = 7). The band intensity of the lipid classes was quantified by ImageJ and normalized to the wild-type mouse sebum lipids.
  - (B) Abundance of triglycerides in the mouse sebum (mg/dL) from 1 cm<sup>2</sup> of hair was measured by colorimetric assay (wild type, *n* = 6; DKO, *n* = 6).
  - (C) Dry weight of sebum lipids from wild-type and DKO mice with or without olive oil supplementation (+oil gavage) (wild type, *n* = 10; DKO, *n* = 14; wild type + oil, *n* = 5; DKO + oil, *n* = 5).
  - (D) Immunofluorescence imaging of CD36 in the dorsal skin of male wild-type and DKO mice, ± olive oil supplementation (scale bars, 50 µm).
  - (E) Dry weight of sebum lipids from wild-type (*Acly*<sup>+/+</sup>) and whole-body Acly-knockout (*Acly*<sup>-/-UBC</sup>) mice (*Acly*<sup>+/+</sup>, *n* = 9; *Acly*<sup>-/-UBC</sup>, *n* = 8).
  - (F–H) Relative abundance of fatty acids derived from (F) sebum (per square-centimeter area of hair), (G) serum (per milliliter), and (H) epidermis (per milligram) of wild-type and DKO mice fed *ad libitum* (wild type, *n* = 6; DKO, *n* = 7), quantified by gas chromatography-mass spectrometry (GC-MS). Data were normalized to the wild-type control of each fatty acid.
- For (A)–(H), data points represent individual mice. Statistical significance was calculated by two-way ANOVA in (C) and unpaired two-sided t tests in (A), (B), and (E–H) (ns, not statistically significant; \**p* ≤ 0.05 and \*\**p* ≤ 0.01).



(legend on next page)

adipose tissues cannot explain the systemic phenotypes of these mice compared to skin-specific *Acly*-knockout mice. Therefore, the skin-extrinsic mechanism(s) that drive more severe systemic changes remains elusive. Given that ZFD exacerbates the phenotypes of *Acly*-knockout skin, we speculate that competition from other *ACLY*-deficient organs for systemic lipids or acetate might account for the more severe phenotypes in whole-body versus skin-specific *Acly*-knockout mice. Indeed, lower circulating NEFAs and sebum production observed in whole-body *Acly*-knockout mice might indicate that interorgan resource competition is a plausible explanation.

Another intriguing observation that will be of interest for further studies is that the eyes develop abnormal phenotypes in the absence of *ACLY*. Modified from SGs, the meibomian glands (MGs) in the eyelids secrete lipids to coat the cornea surface, which minimizes water evaporation and microorganism invasion.<sup>86</sup> MGs also express K14<sup>87</sup>; thus, these structures are targets of TAM-induced gene deletion in mice with skin-specific Cre driver. In this study, we observed dry and irritated eye conditions across mouse models that were present shortly after TAM induction and preceded skin abnormalities, suggesting that MGs are highly sensitive to nucleocytosolic acetyl-CoA levels. Several mouse knockouts of fatty acid elongases display dry eye phenotypes, underscoring the importance of fatty acid elongation for normal MG function.<sup>86</sup> Therefore, our DKO mouse model may be utilized to study the mechanisms of MG dysfunction, which is a multifactorial disease with no effective treatment.

In summary, we have demonstrated that acetyl-CoA metabolism is essential for the maintenance of skin lipids and barrier function, findings that will be relevant to consider if new systemic inhibitors to *ACLY* are developed. We further show that disrupting acetyl-CoA synthesis in the skin exerts profound effects on systemic lipid homeostasis. Since the role of the skin in systemic lipid metabolism has received relatively little attention to date, these findings should prompt further investigation into the mechanisms of metabolic interplay between skin, adipose tissue, and diet.

#### Limitations of the study

The complex phenotype of the model and the essential role of the skin barrier for viability make it challenging to functionally test the multifaceted mechanisms that are engaged to compensate for the loss of *ACLY* and *ACSS2* in the skin. Profiling of serum cyto-

kines may provide additional clues to the key factors regulating adipose lipolysis in this model. In addition, the current study was carried out at room temperature, and experiments under thermoneutral conditions would be informative for defining the contribution of heat loss and thermogenesis responses to these phenotypes. Moreover, we have not formally demonstrated the sources of the fatty acids that sustain sebum production. Isotope labeling experiments would be required to test the movement of fatty acids from diet to adipose and skin, as well as potentially from adipose to skin, coupled with genetic or pharmacological inhibition of lipolysis. Finally, spatial transcriptomics and metabolomics will be useful to better understand the distinct regulation of lipid metabolism and gene expression within each skin compartment.

#### RESOURCE AVAILABILITY

##### Lead contact

Requests for further information and resources and reagents should be directed to and will be fulfilled by the lead contact, Dr. Kathryn E. Weller ([wellenk@upenn.edu](mailto:wellenk@upenn.edu)).

##### Materials availability

All unique reagents generated in this study are available from the [lead contact](#), Dr. Kathryn E. Weller ([wellenk@upenn.edu](mailto:wellenk@upenn.edu)). *Acly*<sup>fl/fl</sup> mice have been reported,<sup>28</sup> and they are available from The Jackson Laboratory under strain name *Acly*<sup>tm1.1Welle</sup>/Mmjjax.

##### Data and code availability

- RNA sequencing data are deposited in GEO under GEO: GSE276591. Lipidomics datasets are included in [Table S1](#) and are deposited in the Metabolomics Workbench under Project DOI: <http://dx.doi.org/10.21228/M88J99> (Project ST003644). Full western blot and TLC scans and source data related to [Figures 1, 2, 3, 4, 5, 6, 7](#), and [S1–S7](#) can be found in [Data S1](#). All other data will be shared by the [lead contact](#), Dr. Kathryn E. Weller ([wellenk@upenn.edu](mailto:wellenk@upenn.edu)), upon request.
- This article does not report any original code.
- Any additional information required to reanalyze the data will be shared by the [lead contact](#) upon request.

#### ACKNOWLEDGMENTS

The authors thank the Penn IDOM Mouse Metabolic Phenotyping Core (supported by grant S10-OD025098 and the Cox Institute), particularly Xiaoyan Yin and Corey Holman, for the metabolic cage and body composition analysis; the Penn Skin Biology and Diseases Resource-Based Center (supported by grant P30AR069589) for TEWL analysis and providing human keratinocytes;

#### Figure 7. Transcriptional profiles of skin lacking both *ACLY* and *ACSS2* reveal changes in inflammatory response, lipid metabolism, and secreted factors

- (A) KEGG pathway analysis by clusterProfiler for epidermis from wild-type (*Acly*<sup>fl/fl</sup>; *Acss2*<sup>fl/fl</sup>) and DKO (*Acly*<sup>ΔKRT14</sup>; *Acss2*<sup>ΔKRT14</sup>) mice at day 12 (12d) post tamoxifen (TAM) induction, with adjusted  $p < 0.05$ .
- (B) Gene set enrichment analysis (GSEA) by clusterProfiler for epidermis from DKO mice compared to wild type at day 21 (21d) post TAM induction, with adjusted  $p < 0.05$ . Plot shows enriched hallmarks.
- (C) Venn diagram of the overlap of the top upregulated genes (adjusted  $p < 0.05$  and log2 fold change threshold of 0.5) in DKO epidermis at days 12 and 21 post TAM induction and a curated list of genes encoding secretory proteins (filtered by subcellular location in the UniProt protein database—see [Table S2](#)).
- (D) Hierarchical clustering heatmap of 62 genes obtained from (C) in epidermis from DKO mice at days 12 and 21. Rows represent individual genes and columns represent biological replicates. Hierarchical clustering was performed using Manhattan distance and the complete-linkage method.
- (E) mRNA expression of selected genes from (D) in the epidermis of wild-type and DKO male mice at day 21 with or without olive oil supplementation (+oil gavage) (wild type,  $n = 7$ ; DKO,  $n = 7$ ; wild type + oil,  $n = 3$ –4; DKO + oil,  $n = 5$ –6). Data were first normalized to *Actin* and then to DKO mice with no gavage.
- (F) Working model of the role of acetyl-CoA metabolism in the skin in local and systemic lipid homeostasis (AcCoA, acetyl-CoA; TAGs, triglycerides; LCFAs, long-chain fatty acids; VLCFAs, very-long-chain fatty acids). Model figure was created with BioRender.
- Statistical significance was calculated by two-way ANOVA in (E) (ns, not statistically significant; \* $p \leq 0.05$ , \*\* $p \leq 0.01$ , \*\*\* $p \leq 0.001$ , and \*\*\*\* $p \leq 0.0001$ ). See also [Figures S6](#) and [S7](#) and [Tables S2](#) and [S3](#).

the Penn Molecular Pathology and Imaging Core for tissue histology; and Pen-  
ing Xu for help with running LC-MS samples for lipidomics. This work was sup-  
ported by NIH grants R01DK116005, R01CA262055, and Ludwig Cancer  
Research grants to K.E.W.; NIH grant R01AR077615 to B.C.C.; and NIH grant  
P30ES01350 to C.M. P.T.T.N. was supported by a Blavatnik Family Foundation  
Fellowship, N.K. by T32-AR-007465, P.C.P. by K00CA245802, L.T.I. by T32-  
CA-115299, H.A.A. by NIH grant K00CA212455, L.V.P. by T32DK007314 and  
a diversity supplement to R01CA262055, J.Y.L. by F30DK126353, and J.C.H.  
by F31AR079845 and T32AR007465.

#### AUTHOR CONTRIBUTIONS

Conceptualization, P.T.T.N., H.A.A., and K.E.W.; methodology, P.T.T.N.,  
H.A.A., C.M., L.T.I., and K.E.W.; formal analysis, P.T.T.N., M.S., N.K.,  
P.C.-P., L.V.P., and G.G.; investigation, P.T.T.N., M.S., N.K., P.C.-P., L.T.I.,  
L.V.P., S.G., J.Y.L., J.C.H., C.W.B., and T.K.; visualization, P.T.T.N., L.V.P.,  
and G.G.; supervision, K.E.W., B.C.C., C.M., X.Y., T.K., and J.T.S.; writing –  
original draft, P.T.T.N. and K.E.W.; writing – review and editing, all authors.

#### DECLARATION OF INTERESTS

K.E.W. is a member of the scientific advisory board of Crescenza Biosciences,  
which is unrelated to the current study. T.K. has a patent filed on using TSLP  
and TSLP-elevating agents for treating obesity and lipid-related conditions.

#### STAR METHODS

Detailed methods are provided in the online version of this paper and include  
the following:

- KEY RESOURCES TABLE
- EXPERIMENTAL MODEL AND STUDY PARTICIPANT DETAILS
  - Animal studies
  - Human primary keratinocyte culture
- METHOD DETAILS
  - Inhibitor treatment and fatty acid supplementation for NHEKs
  - Genotyping
  - Tamoxifen regimen
  - Olive oil gavage
  - Topical treatments
  - Metabolic cage and body composition analyses
  - Behavioral assessments
  - Glucose tolerance test
  - Tissue histology
  - Immunofluorescent staining
  - Epidermal isolation
  - Western blotting
  - Fecal protein extraction
  - RNA extraction
  - RT-qPCR
  - RNA sequencing and analysis
  - Trans epidermal water loss (TEWL)
  - Thin layer chromatography (TLC)
  - Fecal lipid extraction
  - Lipid quantification by colorimetric assays
  - Lipidomics by liquid chromatography-high resolution mass spec-  
trometry (LC-MS)
  - Quantification of fatty acids by fatty acid methyl-esterification  
(FAME) with gas chromatography-mass spectrometry (GC-MS)
  - T cell depletion and flow cytometry
- QUANTIFICATION AND STATISTICAL ANALYSIS

#### SUPPLEMENTAL INFORMATION

Supplemental information can be found online at <https://doi.org/10.1016/j.celrep.2025.115284>.

Received: December 22, 2023

Revised: December 10, 2024

Accepted: January 16, 2025

Published: February 10, 2025

#### REFERENCES

1. Pietrocola, F., Galluzzi, L., Bravo-San Pedro, J.M., Madeo, F., and Kroemer, G. (2015). Acetyl coenzyme A: a central metabolite and second messenger. *Cell Metab.* 21, 805–821. <https://doi.org/10.1016/j.cmet.2015.05.014>
2. Martinez-Reyes, I., and Chandel, N.S. (2020). Mitochondrial TCA cycle metabolites control physiology and disease. *Nat. Commun.* 11, 102. <https://doi.org/10.1038/s41467-019-13668-3>
3. Trefely, S., Lovell, C.D., Snyder, N.W., and Wellen, K.E. (2020). Compartmentalised acyl-CoA metabolism and roles in chromatin regulation. *Mol. Metab.* 38, 100941. <https://doi.org/10.1016/j.molmet.2020.01.005>
4. Pinkosky, S.L., Groot, P.H.E., Lalwani, N.D., and Steinberg, G.R. (2017). Targeting ATP-Citrate Lyase in Hyperlipidemia and Metabolic Disorders. *Trends Mol. Med.* 23, 1047–1063. <https://doi.org/10.1016/j.molmed.2017.09.001>
5. Feng, X., Zhang, L., Xu, S., and Shen, A.Z. (2020). ATP-citrate lyase (ACLY) in lipid metabolism and atherosclerosis: An updated review. *Prog. Lipid Res.* 77, 101006. <https://doi.org/10.1016/j.plipres.2019.101006>
6. Icard, P., Wu, Z., Fournel, L., Coquerel, A., Lincet, H., and Alifano, M. (2020). ATP citrate lyase: A central metabolic enzyme in cancer. *Cancer Lett.* 471, 125–134. <https://doi.org/10.1016/j.canlet.2019.12.010>
7. Markham, A. (2020). Bempedoic Acid: First Approval. *Drugs* 80, 747–753. <https://doi.org/10.1007/s40265-020-01308-w>
8. Nissen, S.E., Lincoff, A.M., Brennan, D., Ray, K.K., Mason, D., Kastelein, J.J.P., Thompson, P.D., Libby, P., Cho, L., Plutzky, J., et al. (2023). Bempedoic Acid and Cardiovascular Outcomes in Statin-Intolerant Patients. *N. Engl. J. Med.* 388, 1353–1364. <https://doi.org/10.1056/NEJMoa2215024>
9. Hatzivassiliou, G., Zhao, F., Bauer, D.E., Andreadis, C., Shaw, A.N., Dhanak, D., Hingorani, S.R., Tuveson, D.A., and Thompson, C.B. (2005). ATP citrate lyase inhibition can suppress tumor cell growth. *Cancer Cell* 8, 311–321. <https://doi.org/10.1016/j.ccr.2005.09.008>
10. Migita, T., Narita, T., Nomura, K., Miyagi, E., Inazuka, F., Matsuura, M., Ushijima, M., Mashima, T., Seimiya, H., Satoh, Y., et al. (2008). ATP citrate lyase: activation and therapeutic implications in non-small cell lung cancer. *Cancer Res.* 68, 8547–8554. <https://doi.org/10.1158/0008-5472.CAN-08-1235>
11. Lin, R., Tao, R., Gao, X., Li, T., Zhou, X., Guan, K.L., Xiong, Y., and Lei, Q.Y. (2013). Acetylation stabilizes ATP-citrate lyase to promote lipid biosynthesis and tumor growth. *Mol. Cell* 51, 506–518. <https://doi.org/10.1016/j.molcel.2013.07.002>
12. Shah, S., Carriéau, W.J., Li, J., Campbell, S.L., Kopinski, P.K., Lim, H.W., Daurio, N., Trefely, S., Won, K.J., Wallace, D.C., et al. (2016). Targeting ACLY sensitizes castration-resistant prostate cancer cells to AR antagonism by impinging on an ACLY-AMPK-AR feedback mechanism. *Oncotarget* 7, 43713–43730. <https://doi.org/10.18633/oncotarget.9666>
13. Zhang, C., Liu, J., Huang, G., Zhao, Y., Yue, X., Wu, H., Li, J., Zhu, J., Shen, Z., Haffty, B.G., et al. (2016). Cullin3-KLHL25 ubiquitin ligase targets ACLY for degradation to inhibit lipid synthesis and tumor progression. *Genes Dev.* 30, 1956–1970. <https://doi.org/10.1101/gad.283283.116>
14. Carrer, A., Trefely, S., Zhao, S., Campbell, S.L., Norgard, R.J., Schultz, K.C., Sidoli, S., Parrish, J.L.D., Affronti, H.C., Sivanand, S., et al. (2019). Acetyl-CoA Metabolism Supports Multistep Pancreatic Tumorigenesis. *Cancer Discov.* 9, 416–435. <https://doi.org/10.1158/2159-8290.CD-18-0567>
15. Wei, X., Shi, J., Lin, Q., Ma, X., Pang, Y., Mao, H., Li, R., Lu, W., Wang, Y., and Liu, P. (2021). Targeting ACLY Attenuates Tumor Growth and Acquired Cisplatin Resistance in Ovarian Cancer by Inhibiting the

- PI3K-AKT Pathway and Activating the AMPK-ROS Pathway. *Front. Oncol.* 11, 642229. <https://doi.org/10.3389/fonc.2021.642229>.
16. Huang, S.S., Tsai, C.H., Kuo, C.Y., Li, Y.S., and Cheng, S.P. (2022). ACLY inhibitors induce apoptosis and potentiate cytotoxic effects of sorafenib in thyroid cancer cells. *Endocrine* 78, 85–94. <https://doi.org/10.1007/s12020-022-03124-6>.
  17. Xiang, W., Lv, H., Xing, F., Sun, X., Ma, Y., Wu, L., Lv, G., Zong, Q., Wang, L., Wu, Z., et al. (2023). Inhibition of ACLY overcomes cancer immunotherapy resistance via polyunsaturated fatty acids peroxidation and cGAS-STING activation. *Sci. Adv.* 9, eadi2465. <https://doi.org/10.1126/sciadv.adl2465>.
  18. Comerford, S.A., Huang, Z., Du, X., Wang, Y., Cai, L., Witkiewicz, A.K., Walters, H., Tantawy, M.N., Fu, A., Manning, H.C., et al. (2014). Acetate dependence of tumors. *Cell* 159, 1591–1602. <https://doi.org/10.1016/j.cell.2014.11.020>.
  19. Schug, Z.T., Peck, B., Jones, D.T., Zhang, Q., Grosskurth, S., Alam, I.S., Goodwin, L.M., Smethurst, E., Mason, S., Blyth, K., et al. (2015). Acetyl-CoA synthetase 2 promotes acetate utilization and maintains cancer cell growth under metabolic stress. *Cancer Cell* 27, 57–71. <https://doi.org/10.1016/j.ccr.2014.12.002>.
  20. Li, Z., Liu, H., He, J., Wang, Z., Yin, Z., You, G., Wang, Z., Davis, R.E., Lin, P., Bergsagel, P.L., et al. (2021). Acetyl-CoA Synthetase 2: A Critical Linkage in Obesity-Induced Tumorigenesis in Myeloma. *Cell Metab.* 33, 78–93.e7. <https://doi.org/10.1016/j.cmet.2020.12.011>.
  21. Miller, K.D., Pniewski, K., Perry, C.E., Papp, S.B., Shaffer, J.D., Velasco-Silva, J.N., Casciano, J.C., Aramburu, T.M., Srikanth, Y.V.V., Cassel, J., et al. (2021). Targeting ACSS2 with a Transition-State Mimetic Inhibits Triple-Negative Breast Cancer Growth. *Cancer Res.* 81, 1252–1264. <https://doi.org/10.1158/0008-5472.CAN-20-1847>.
  22. Que, D., Kuang, F., Kang, R., Tang, D., and Liu, J. (2023). ACSS2-mediated NF-κappaB activation promotes alkaliptosis in human pancreatic cancer cells. *Sci. Rep.* 13, 1483. <https://doi.org/10.1038/s41598-023-28261-4>.
  23. Garcia, J.A., Chen, R., Xu, M., Comerford, S.A., Hammer, R.E., Melton, S.D., and Feagins, L.A. (2023). Acss2/HIF-2 signaling facilitates colon cancer growth and metastasis. *PLoS One* 18, e0282223. <https://doi.org/10.1371/journal.pone.0282223>.
  24. Miller, K.D., O'Connor, S., Pniewski, K.A., Kannan, T., Acosta, R., Mirji, G., Papp, S., Hulse, M., Mukha, D., Hlavaty, S.I., et al. (2023). Acetate acts as a metabolic immunomodulator by bolstering T-cell effector function and potentiating antitumor immunity in breast cancer. *Nat Cancer* 4, 1491–1507. <https://doi.org/10.1038/s43018-023-00636-6>.
  25. Huang, Z., Zhang, M., Plec, A.A., Estill, S.J., Cai, L., Repa, J.J., McKnight, S.L., and Tu, B.P. (2018). ACSS2 promotes systemic fat storage and utilization through selective regulation of genes involved in lipid metabolism. *Proc. Natl. Acad. Sci. USA* 115, E9499–E9506. <https://doi.org/10.1073/pnas.1806635115>.
  26. Li, S., de Camargo Correia, G.S., Wang, J., Manochakian, R., Zhao, Y., and Lou, Y. (2023). Emerging Targeted Therapies in Advanced Non-Small-Cell Lung Cancer. *Cancers* 15, 2899. <https://doi.org/10.3390/cancers15112899>.
  27. Beigneux, A.P., Kosinski, C., Gavino, B., Horton, J.D., Skarnes, W.C., and Young, S.G. (2004). ATP-citrate lyase deficiency in the mouse. *J. Biol. Chem.* 279, 9557–9564. <https://doi.org/10.1074/jbc.M310512200>.
  28. Zhao, S., Torres, A., Henry, R.A., Trefely, S., Wallace, M., Lee, J.V., Carrer, A., Sengupta, A., Campbell, S.L., Kuo, Y.M., et al. (2016). ATP-Citrate Lyase Controls a Glucose-to-Acetate Metabolic Switch. *Cell Rep.* 17, 1037–1052. <https://doi.org/10.1016/j.celrep.2016.09.069>.
  29. Martinez Calejman, C., Trefely, S., Entwistle, S.W., Luciano, A., Jung, S.M., Hsiao, W., Torres, A., Hung, C.M., Li, H., Snyder, N.W., et al. (2020). mTORC2-AKT signaling to ATP-citrate lyase drives brown adipogenesis and de novo lipogenesis. *Nat. Commun.* 11, 575. <https://doi.org/10.1038/s41467-020-14430-w>.
  30. Korobkina, E.D., Calejman, C.M., Haley, J.A., Kelly, M.E., Li, H., Gaughan, M., Chen, Q., Pepper, H.L., Ahmad, H., Boucher, A., et al. (2024). Brown fat ATP-citrate lyase links carbohydrate availability to thermogenesis and guards against metabolic stress. *Nat. Metab.* 6, 2187–2202. <https://doi.org/10.1038/s42255-024-01143-3>.
  31. Zhao, S., Jang, C., Liu, J., Uehara, K., Gilbert, M., Izzo, L., Zeng, X., Trefely, S., Fernandez, S., Carrer, A., et al. (2020). Dietary fructose feeds hepatic lipogenesis via microbiota-derived acetate. *Nature* 579, 586–591. <https://doi.org/10.1038/s41586-020-2101-7>.
  32. Morrow, M.R., Batchuluun, B., Wu, J., Ahmadi, E., Leroux, J.M., Mohammadi-Shemirani, P., Desjardins, E.M., Wang, Z., Tsakiridis, E.E., Lavoie, D.C.T., et al. (2022). Inhibition of ATP-citrate lyase improves NASH, liver fibrosis, and dyslipidemia. *Cell Metab.* 34, 919–936.e8. <https://doi.org/10.1016/j.cmet.2022.05.004>.
  33. Yenilmez, B., Kelly, M., Zhang, G.F., Wetoska, N., Ilkayeva, O.R., Min, K., Rowland, L., DiMarzio, C., He, W., Raymond, N., et al. (2022). Paradoxical activation of transcription factor SREBP1c and de novo lipogenesis by hepatocyte-selective ATP-citrate lyase depletion in obese mice. *J. Biol. Chem.* 298, 102401. <https://doi.org/10.1016/j.jbc.2022.102401>.
  34. Liu, J.Y., Kuna, R.S., Pinheiro, L.V., Nguyen, P.T.T., Welles, J.E., Drummond, J.M., Murali, N., Sharma, P.V., Supplee, J.G., Shiue, M., et al. (2025). Bempedoic acid suppresses diet-induced hepatic steatosis independently of ATP-citrate lyase. *Cell Metab.* 37, 239–254.e7. <https://doi.org/10.1016/j.cmet.2024.10.014>.
  35. Baardman, J., Verberk, S.G.S., van der Velden, S., Gijbels, M.J.J., van Roomen, C.P.P.A., Sluimer, J.C., Broos, J.Y., Griffith, G.R., Prange, K.H.M., van Weeghel, M., et al. (2020). Macrophage ATP citrate lyase deficiency stabilizes atherosclerotic plaques. *Nat. Commun.* 11, 6296. <https://doi.org/10.1038/s41467-020-20141-z>.
  36. Greenwood, D.L., Ramsey, H.E., Nguyen, P.T.T., Patterson, A.R., Voss, K., Bader, J.E., Sugiura, A., Bacigalupa, Z.A., Schaefer, S., Ye, X., et al. (2022). Acyl Deficiency Enhances Myelopoiesis through Acetyl Coenzyme A and Metabolic-Epigenetic Cross-Talk. *Immunohorizons* 6, 837–850. <https://doi.org/10.4049/immunohorizons.2200086>.
  37. Noe, J.T., Rendon, B.E., Geller, A.E., Conroy, L.R., Morrissey, S.M., Young, L.E.A., Bruntz, R.C., Kim, E.J., Wise-Mitchell, A., Barbosa de Souza Rizzo, M., et al. (2021). Lactate supports a metabolic-epigenetic link in macrophage polarization. *Sci. Adv.* 7, eabi8602. <https://doi.org/10.1126/sciadv.abi8602>.
  38. Kaymak, I., Watson, M.J., Oswald, B.M., Ma, S., Johnson, B.K., DeCamp, L.M., Mabvukure, B.M., Luda, K.M., Ma, E.H., Lau, K., et al. (2024). ACLY and ACSS2 link nutrient-dependent chromatin accessibility to CD8 T cell effector responses. *J. Exp. Med.* 221, e20231820. <https://doi.org/10.1084/jem.20231820>.
  39. Ma, S., Dahabieh, M.S., Mann, T.H., Zhao, S., McDonald, B., Song, W.S., Chung, H.K., Farsakoglu, Y., Garcia-Rivera, L., Hoffmann, F.A., et al. (2024). Nutrient-driven histone code determines exhausted CD8(+) T cell fates. *Science* 387, eadj3020. <https://doi.org/10.1126/science.adj3020>.
  40. Feingold, K.R. (2007). Thematic review series: skin lipids. The role of epidermal lipids in cutaneous permeability barrier homeostasis. *J. Lipid Res.* 48, 2531–2546. <https://doi.org/10.1194/jlr.R700013-JLR200>.
  41. Smith, K.R., and Thiboutot, D.M. (2008). Thematic review series: skin lipids. Sebaceous gland lipids: friend or foe? *J. Lipid Res.* 49, 271–281. <https://doi.org/10.1194/jlr.R700015-JLR200>.
  42. Lalonde, R., and Strazielle, C. (2011). Brain regions and genes affecting limb-clasping responses. *Brain Res. Rev.* 67, 252–259. <https://doi.org/10.1016/j.brainresrev.2011.02.005>.
  43. Bouwstra, J.A., and Ponec, M. (2006). The skin barrier in healthy and diseased state. *Biochim. Biophys. Acta* 1758, 2080–2095. <https://doi.org/10.1016/j.bbamem.2006.06.021>.
  44. Joost, S., Annusver, K., Jacob, T., Sun, X., Dalessandri, T., Sivan, U., Sequeira, I., Sandberg, R., and Kasper, M. (2020). The Molecular Anatomy of Mouse Skin during Hair Growth and Rest. *Cell Stem Cell* 26, 441–457.e7. <https://doi.org/10.1016/j.stem.2020.01.012>.

45. Yano, K., Brown, L.F., and Detmar, M. (2001). Control of hair growth and follicle size by VEGF-mediated angiogenesis. *J. Clin. Invest.* 107, 409–417. <https://doi.org/10.1172/JCI11317>.
46. Schneider, M.R., Schmidt-Ullrich, R., and Paus, R. (2009). The hair follicle as a dynamic miniorgan. *Curr. Biol.* 19, R132–R142. <https://doi.org/10.1016/j.cub.2008.12.005>.
47. Foster, A.R., Nicu, C., Schneider, M.R., Hinde, E., and Paus, R. (2018). Dermal white adipose tissue undergoes major morphological changes during the spontaneous and induced murine hair follicle cycling: a reappraisal. *Arch. Dermatol. Res.* 310, 453–462. <https://doi.org/10.1007/s00403-018-1831-y>.
48. Muller-Rover, S., Handjiski, B., van der Veen, C., Eichmuller, S., Foitzik, K., McKay, I.A., Stenn, K.S., and Paus, R. (2001). A comprehensive guide for the accurate classification of murine hair follicles in distinct hair cycle stages. *J. Invest. Dermatol.* 117, 3–15. <https://doi.org/10.1046/j.0022-202x.2001.01377.x>.
49. Izzo, L.T., Affronti, H.C., and Wollen, K.E. (2021). The Bidirectional Relationship Between Cancer Epigenetics and Metabolism. *Annu. Rev. Cancer Biol.* 5, 235–257. <https://doi.org/10.1146/annurev-cancerbio-070820-035832>.
50. Blanpain, C., and Fuchs, E. (2006). Epidermal stem cells of the skin. *Annu. Rev. Cell Dev. Biol.* 22, 339–373. <https://doi.org/10.1146/annurev.cellbio.22.010305.104357>.
51. Liarte, S., Bernabe-Garcia, A., and Nicolas, F.J. (2020). Role of TGF-beta in Skin Chronic Wounds: A Keratinocyte Perspective. *Cells* 9, 306. <https://doi.org/10.3390/cells9020306>.
52. Sakers, A., De Siqueira, M.K., Seale, P., and Villanueva, C.J. (2022). Adipose-tissue plasticity in health and disease. *Cell* 185, 419–446. <https://doi.org/10.1016/j.cell.2021.12.016>.
53. Pastar, I., Stojadinovic, O., Yin, N.C., Ramirez, H., Nusbaum, A.G., Sawaya, A., Patel, S.B., Khalid, L., Isseroff, R.R., and Tomic-Canic, M. (2014). Epithelialization in Wound Healing: A Comprehensive Review. *Adv. Wound Care* 3, 445–464. <https://doi.org/10.1089/wound.2013.0473>.
54. Hayes, M.D., Ward, S., Crawford, G., Seoane, R.C., Jackson, W.D., Kipping, D., Voehringer, D., Dunn-Walters, D., and Strid, J. (2020). Inflammation-induced IgE promotes epithelial hyperplasia and tumour growth. *Elife* 9, e51862. <https://doi.org/10.7554/elife.51862>.
55. Duncan, R.E., Ahmadian, M., Jaworski, K., Sarkadi-Nagy, E., and Sul, H.S. (2007). Regulation of lipolysis in adipocytes. *Annu. Rev. Nutr.* 27, 79–101. <https://doi.org/10.1146/annurev.nutr.27.061406.093734>.
56. Sampath, H., Flowers, M.T., Liu, X., Paton, C.M., Sullivan, R., Chu, K., Zhao, M., and Ntambi, J.M. (2009). Skin-specific deletion of stearoyl-CoA desaturase-1 alters skin lipid composition and protects mice from high fat diet-induced obesity. *J. Biol. Chem.* 284, 19961–19973. <https://doi.org/10.1074/jbc.M109.014225>.
57. Narvaez, C.J., Matthews, D., Broun, E., Chan, M., and Welsh, J. (2009). Lean phenotype and resistance to diet-induced obesity in vitamin D receptor knockout mice correlates with induction of uncoupling protein-1 in white adipose tissue. *Endocrinology* 150, 651–661. <https://doi.org/10.1210/en.2008-1118>.
58. Ikeda, K., and Yamada, T. (2020). UCP1 Dependent and Independent Thermogenesis in Brown and Beige Adipocytes. *Front. Endocrinol.* 11, 498. <https://doi.org/10.3389/fendo.2020.00498>.
59. Kihara, A. (2012). Very long-chain fatty acids: elongation, physiology and related disorders. *J. Biochem.* 152, 387–395. <https://doi.org/10.1093/jb/mvs105>.
60. Jump, D.B. (2009). Mammalian fatty acid elongases. *Methods Mol. Biol.* 579, 375–389. [https://doi.org/10.1007/978-1-60761-322-0\\_19](https://doi.org/10.1007/978-1-60761-322-0_19).
61. Esler, W.P., Tesz, G.J., Hellerstein, M.K., Beysen, C., Sivamani, R., Turner, S.M., Watkins, S.M., Amor, P.A., Carvajal-Gonzalez, S., Geoly, F.J., et al. (2019). Human sebum requires de novo lipogenesis, which is increased in acne vulgaris and suppressed by acetyl-CoA carboxylase inhibition. *Sci. Transl. Med.* 11, eaau8465. <https://doi.org/10.1126/scitranslmed.aau8465>.
62. Lin, T.K., Zhong, L., and Santiago, J.L. (2017). Anti-Inflammatory and Skin Barrier Repair Effects of Topical Application of Some Plant Oils. *Int. J. Mol. Sci.* 19, 70. <https://doi.org/10.3390/ijms19010070>.
63. Choa, R., Tohyama, J., Wada, S., Meng, H., Hu, J., Okumura, M., May, R.M., Robertson, T.F., Pai, R.A.L., Nace, A., et al. (2021). Thymic stromal lymphopoietin induces adipose loss through sebum hypersecretion. *Science* 373, eabd2893. <https://doi.org/10.1126/science.abd2893>.
64. Dajnoki, Z., Béke, G., Kapitány, A., Mócsai, G., Gáspár, K., Rühl, R., Hendrik, Z., Juhász, I., Zouboulis, C.C., Bácsi, A., et al. (2017). Sebaceous Gland-Rich Skin Is Characterized by TSLP Expression and Distinct Immune Surveillance Which Is Disturbed in Rosacea. *J. Invest. Dermatol.* 137, 1114–1125. <https://doi.org/10.1016/j.jid.2016.12.025>.
65. Lefevre-Utile, A., Braun, C., Haftek, M., and Aubin, F. (2021). Five Functional Aspects of the Epidermal Barrier. *Int. J. Mol. Sci.* 22, 11676. <https://doi.org/10.3390/ijms22111676>.
66. Kruse, V., Neess, D., and Færgeman, N.J. (2017). The Significance of Epidermal Lipid Metabolism in Whole-Body Physiology. *Trends Endocrinol. Metab.* 28, 669–683. <https://doi.org/10.1016/j.tem.2017.06.001>.
67. Zwara, A., Wertheim-Tysarska, K., and Mika, A. (2021). Alterations of Ultra Long-Chain Fatty Acids in Hereditary Skin Diseases—Review Article. *Front. Med.* 8, 730855. <https://doi.org/10.3389/fmed.2021.730855>.
68. Westerberg, R., Tvrđik, P., Undén, A.B., Månnsson, J.E., Norlén, L., Jakobsson, A., Holleran, W.H., Elias, P.M., Asadi, A., Flodby, P., et al. (2004). Role for ELOVL3 and fatty acid chain length in development of hair and skin function. *J. Biol. Chem.* 279, 5621–5629. <https://doi.org/10.1074/jbc.M310529200>.
69. Sassa, T., Ohno, Y., Suzuki, S., Nomura, T., Nishioka, C., Kashiwagi, T., Hirayama, T., Akiyama, M., Taguchi, R., Shimizu, H., et al. (2013). Impaired epidermal permeability barrier in mice lacking elovl1, the gene responsible for very-long-chain fatty acid production. *Mol. Cell Biol.* 33, 2787–2796. <https://doi.org/10.1128/MCB.00192-13>.
70. Vasireddy, V., Uchida, Y., Salem, N., Jr., Kim, S.Y., Mandal, M.N.A., Reddy, G.B., Bodepudi, R., Alderson, N.L., Brown, J.C., Hama, H., et al. (2007). Loss of functional ELOVL4 depletes very long-chain fatty acids (> or =C28) and the unique omega-O-acylceramides in skin leading to neonatal death. *Hum. Mol. Genet.* 16, 471–482. <https://doi.org/10.1093/hmg/ddl480>.
71. Jennemann, R., Rabionet, M., Gorgas, K., Epstein, S., Dalpke, A., Rothermel, U., Bayerle, A., van der Hoeven, F., Imgrund, S., Kirsch, J., et al. (2012). Loss of ceramide synthase 3 causes lethal skin barrier disruption. *Hum. Mol. Genet.* 21, 586–608. <https://doi.org/10.1093/hmg/ddr494>.
72. Miyamoto, M., Itoh, N., Sawai, M., Sassa, T., and Kihara, A. (2020). Severe Skin Permeability Barrier Dysfunction in Knockout Mice Deficient in a Fatty Acid omega-Hydroxylase Crucial to Acylceramide Production. *J. Invest. Dermatol.* 140, 319–326.e4. <https://doi.org/10.1016/j.jid.2019.07.689>.
73. Falchook, G., Infante, J., Arkenau, H.T., Patel, M.R., Dean, E., Borazanci, E., Brenner, A., Cook, N., Lopez, J., Pant, S., et al. (2021). First-in-human study of the safety, pharmacokinetics, and pharmacodynamics of first-in-class fatty acid synthase inhibitor TVB-2640 alone and with a taxane in advanced tumors. *EClinicalMedicine* 34, 100797. <https://doi.org/10.1016/j.eclim.2021.100797>.
74. Bloksgaard, M., Bek, S., Marcher, A.B., Neess, D., Brewer, J., Hannibal-Bach, H.K., Helledie, T., Fenger, C., Due, M., Berzina, Z., et al. (2012). The acyl-CoA binding protein is required for normal epidermal barrier function in mice. *J. Lipid Res.* 53, 2162–2174. <https://doi.org/10.1194/jlr.M029553>.
75. Neess, D., Bek, S., Bloksgaard, M., Marcher, A.B., Færgeman, N.J., and Mandrup, S. (2013). Delayed hepatic adaptation to weaning in ACBP-/mice is caused by disruption of the epidermal barrier. *Cell Rep.* 5, 1403–1412. <https://doi.org/10.1016/j.celrep.2013.11.010>.
76. Neess, D., Kruse, V., Marcher, A.B., Wæde, M.R., Vistisen, J., Møller, P.M., Petersen, R., Brewer, J.R., Ma, T., Colleluori, G., et al. (2021). Epidermal Acyl-CoA-binding protein is indispensable for systemic energy

- homeostasis. *Mol. Metab.* 44, 101144. <https://doi.org/10.1016/j.molmet.2020.101144>.
77. Zadravec, D., Brolinson, A., Fisher, R.M., Carneheim, C., Csikasz, R.I., Bertrand-Michel, J., Borén, J., Guillou, H., Rudling, M., and Jacobsson, A. (2010). Ablation of the very-long-chain fatty acid elongase ELOVL3 in mice leads to constrained lipid storage and resistance to diet-induced obesity. *FASEB J.* 24, 4366–4377. <https://doi.org/10.1096/fj.09-152298>.
  78. Chen, H.C., Smith, S.J., Tow, B., Elias, P.M., and Farese, R.V., Jr. (2002). Leptin modulates the effects of acyl CoA:diacylglycerol acyltransferase deficiency on murine fur and sebaceous glands. *J. Clin. Invest.* 109, 175–181. <https://doi.org/10.1172/JCI13880>.
  79. Riley, N., Kasza, I., Hermmsmeyer, I.D.K., Trautman, M.E., Barrett-Wilt, G., Jain, R., Simcox, J.A., Yen, C.L.E., MacDougald, O.A., Lamming, D.W., and Alexander, C.M. (2024). Dietary lipid is largely deposited in skin and rapidly affects insulating properties. *Res. Sq.* rs.3.rs-3957002. <https://doi.org/10.21203/rs.3.rs-3957002/v1>.
  80. Geyer, P.E., Wewer Albrechtsen, N.J., Tyanova, S., Grassl, N., Iepsen, E.W., Lundgren, J., Madsbad, S., Holst, J.J., Torekov, S.S., and Mann, M. (2016). Proteomics reveals the effects of sustained weight loss on the human plasma proteome. *Mol. Syst. Biol.* 12, 901. <https://doi.org/10.1525/msb.20167357>.
  81. Harney, D.J., Hutchison, A.T., Hatchwell, L., Humphrey, S.J., James, D.E., Hocking, S., Heilbronn, L.K., and Larance, M. (2019). Proteomic Analysis of Human Plasma during Intermittent Fasting. *J. Proteome Res.* 18, 2228–2240. <https://doi.org/10.1021/acs.jproteome.9b00090>.
  82. Figarska, S.M., Rigdon, J., Ganna, A., Elmståhl, S., Lind, L., Gardner, C.D., and Ingelsson, E. (2020). Proteomic profiles before and during weight loss: Results from randomized trial of dietary intervention. *Sci. Rep.* 10, 7913. <https://doi.org/10.1038/s41598-020-64636-7>.
  83. Vernardis, S.I., Demichev, V., Lemke, O., Grüning, N.M., Messner, C., White, M., Pietzner, M., Peluso, A., Collet, T.H., Henning, E., et al. (2023). The Impact of Acute Nutritional Interventions on the Plasma Proteome. *J. Clin. Endocrinol. Metab.* 108, 2087–2098. <https://doi.org/10.1210/clinem/dgad031>.
  84. Gomez-Garcia, I., Trepiana, J., Fernandez-Quintela, A., Giralt, M., and Portillo, M.P. (2022). Sexual Dimorphism in Brown Adipose Tissue Activation and White Adipose Tissue Browning. *Int. J. Mol. Sci.* 23, 8250. <https://doi.org/10.3390/ijms23158250>.
  85. Markussen, L.K., Rondini, E.A., Johansen, O.S., Madsen, J.G.S., Sustarsic, E.G., Marcher, A.B., Hansen, J.B., Gerhart-Hines, Z., Granneman, J.G., and Mandrup, S. (2022). Lipolysis regulates major transcriptional programs in brown adipocytes. *Nat. Commun.* 13, 3956. <https://doi.org/10.1038/s41467-022-31525-8>.
  86. Sun, M., Moreno, I.Y., Dang, M., and Coulson-Thomas, V.J. (2020). Meibomian Gland Dysfunction: What Have Animal Models Taught Us? *Int. J. Mol. Sci.* 21, 8822. <https://doi.org/10.3390/ijms21228822>.
  87. Call, M., Fischesser, K., Lunn, M.O., and Kao, W.W.Y. (2016). A unique lineage gives rise to the meibomian gland. *Mol. Vis.* 22, 168–176.
  88. Huber, W., Carey, V.J., Gentleman, R., Anders, S., Carlson, M., Carvalho, B.S., Bravo, H.C., Davis, S., Gatto, L., Girke, T., et al. (2015). Orchestrating high-throughput genomic analysis with Bioconductor. *Nat. Methods* 12, 115–121. <https://doi.org/10.1038/nmeth.3252>.
  89. Subramanian, A., Tamayo, P., Mootha, V.K., Mukherjee, S., Ebert, B.L., Gillette, M.A., Paulovich, A., Pomeroy, S.L., Golub, T.R., Lander, E.S., and Mesirov, J.P. (2005). Gene set enrichment analysis: a knowledge-based approach for interpreting genome-wide expression profiles. *Proc. Natl. Acad. Sci. USA* 102, 15545–15550. <https://doi.org/10.1073/pnas.0506580102>.
  90. Schneider, C.A., Rasband, W.S., and Eliceiri, K.W. (2012). NIH Image to ImageJ: 25 years of image analysis. *Nat. Methods* 9, 671–675. <https://doi.org/10.1038/nmeth.2089>.
  91. Ruzankina, Y., Pinzon-Guzman, C., Asare, A., Ong, T., Pontano, L., Cotarelis, G., Zediak, V.P., Velez, M., Bhandoola, A., and Brown, E.J. (2007). Deletion of the developmentally essential gene ATR in adult mice leads to age-related phenotypes and stem cell loss. *Cell Stem Cell* 1, 113–126. <https://doi.org/10.1016/j.stem.2007.03.002>.
  92. Vasioukhin, V., Degenstein, L., Wise, B., and Fuchs, E. (1999). The magical touch: genome targeting in epidermal stem cells induced by tamoxifen application to mouse skin. *Proc. Natl. Acad. Sci. USA* 96, 8551–8556. <https://doi.org/10.1073/pnas.96.15.8551>.
  93. Eguchi, J., Wang, X., Yu, S., Kershaw, E.E., Chiu, P.C., Dushay, J., Estall, J.L., Klein, U., Maratos-Flier, E., and Rosen, E.D. (2011). Transcriptional control of adipose lipid handling by IRF4. *Cell Metab.* 13, 249–259. <https://doi.org/10.1016/j.cmet.2011.02.005>.
  94. Truett, G.E., Heeger, P., Mynatt, R.L., Truett, A.A., Walker, J.A., and Warman, M.L. (2000). Preparation of PCR-quality mouse genomic DNA with hot sodium hydroxide and tris (HotSHOT). *Biotechniques* 29, 52–54. <https://doi.org/10.2144/00291bm09>.
  95. Weir, J.B. (1949). New methods for calculating metabolic rate with special reference to protein metabolism. *J. Physiol.* 109, 1–9. <https://doi.org/10.1113/jphysiol.1949.sp004363>.
  96. Deacon, R.M.J. (2013). Measuring motor coordination in mice. *J. Vis. Exp.* e2609. <https://doi.org/10.3791/2609>.
  97. Kraus, D., Yang, Q., and Kahn, B.B. (2015). Lipid Extraction from Mouse Feces. *Bio. Protoc.* 5, e1375. <https://doi.org/10.21769/bioprotoc.1375>.
  98. Dobin, A., Davis, C.A., Schlesinger, F., Drenkow, J., Zaleski, C., Jha, S., Batut, P., Chaisson, M., and Gingeras, T.R. (2013). STAR: ultrafast universal RNA-seq aligner. *Bioinformatics* 29, 15–21. <https://doi.org/10.1093/bioinformatics/bts635>.
  99. Love, M.I., Huber, W., and Anders, S. (2014). Moderated estimation of fold change and dispersion for RNA-seq data with DESeq2. *Genome Biol.* 15, 550. <https://doi.org/10.1186/s13059-014-0550-8>.

## STAR★METHODS

### KEY RESOURCES TABLE

REAGENT or RESOURCE	SOURCE	IDENTIFIER
<b>Antibodies</b>		
Mouse monoclonal anti $\alpha$ -TUBULIN	Millipore	Cat#T6199; RRID: AB_477583
Mouse monoclonal anti-CD45	Novus Biologicals	Cat#NB500-319; RRID: AB_10001403
Mouse monoclonal anti-K14	Abcam	Cat#ab7800; RRID: AB_306091
Rabbit polyclonal anti-ACLY (Western blot)	Proteintech	Cat#15421-1-AP; RRID: AB_2223741
Rabbit monoclonal anti-ACLY (immunofluorescent staining)	Abcam	Cat#ab40793; RRID: AB_722533
Rabbit monoclonal anti-AceCS1 (ACSS2)	Cell Signaling Technology	Cat#3658; RRID: AB_2222710
Rabbit polyclonal anti-acetylated histone H3	Millipore	Cat#06-599; RRID: AB_2115283
Rabbit polyclonal anti-acetylated histone H4	Millipore	Cat#06-866; RRID: AB_310270
Rabbit polyclonal anti-CD3	Abcam	Cat#ab5690; RRID: AB_305055
Rabbit polyclonal anti-CD36	Novus Biologicals	Cat#NB400-144; RRID: AB_10003498
Rabbit polyclonal anti-IVL	BioLegend	Cat#924401; RRID: AB_2565452
Rabbit monoclonal anti-K10	Abcam	Cat#ab76318; RRID: AB_1523465
Rabbit polyclonal anti-Ki67	Abcam	Cat#ab15580; RRID: AB_443209
Rabbit polyclonal anti-LOR	Abcam	Cat#ab85679; RRID: AB_2134912
Rabbit polyclonal anti-pHSL (Ser563)	Cell Signaling Technology	Cat#4139; RRID: AB_2135495
Rabbit monoclonal anti-S6	Cell Signaling Technology	Cat#2217; RRID: AB_331355
Rat monoclonal anti-mouse CD4, Brilliant Violet 650™	BioLegend	Cat#100555; RRID: AB_2562098
Rat monoclonal anti-mouse CD8 $\alpha$ , PE/Cyanine7	BioLegend	Cat#100722; RRID: AB_312761
Rat monoclonal anti-mouse CD45, Alexa Fluor® 700	BioLegend	Cat#103128; RRID: AB_493715
InVivoMAb rat IgG2b isotype control	Bio X Cell	Cat#BE0090; RRID: AB_1107780
InVivoMAb rat monoclonal anti-mouse CD4	Bio X Cell	Cat#BE0003-1; RRID: AB_1107642
InVivoMAb rat monoclonal anti-mouse CD8 $\alpha$	Bio X Cell	Cat#BE0061; RRID: AB_1125541
Donkey polyclonal anti-mouse IgG secondary, Alexa Fluor™ 555	Invitrogen	Cat#A31570; RRID: AB_2536180
Donkey polyclonal anti-rabbit IgG secondary, Alexa Fluor™ 488	Invitrogen	Cat#A21206; RRID: AB_2535792
Goat anti-mouse IgG secondary, IRDye® 680RD	LI-COR Biosciences	Cat#925-68070; RRID: AB_2651128
Goat anti-rabbit IgG secondary, IRDye® 800CW	LI-COR Biosciences	Cat#926-32211; RRID: AB_621843
<b>Biological samples</b>		
Primary human keratinocytes	Penn Skin Biology and Diseases Resource-based Center (SBDRC)	SBDRC: 5148, 5150, 5152, 5159, 5160, 5161
<b>Chemicals, peptides, and recombinant proteins</b>		
4% paraformaldehyde	Thermo Fisher	Cat#AAJ19943K2
Antibiotic-antimycotic	Thermo Fisher	Cat#15240062
BSA	Bioworld	Cat#22070023
BMS-30314	Tocris Bioscience	Cat#4609

(Continued on next page)

**Continued**

REAGENT or RESOURCE	SOURCE	IDENTIFIER
Ceramide/Sphingoid mixture I	Avanti Polar Lipids	Cat#LM6002
Cupric sulfate	Sigma-Aldrich	Cat#451657
DAPI	Sigma-Aldrich	Cat#D9542
D-glucose	Sigma-Aldrich	Cat#G8270
Dispase	Corning	Cat#354235
Donkey serum	Sigma-Aldrich	Cat#D9663
DMSO	Sigma-Aldrich	Cat#D2650
Ethanol	Decon Laboratories	Cat#2716
Human keratinocyte growth supplement	Thermo Fisher	Cat#S0015
Keratinocyte serum-free medium (SFM)	Thermo Fisher	Cat#17005042
Medium 154	Thermo Fisher	Cat#M154500
Non-polar lipid mixture 1	Matreya	Cat#1129
Oleic acids	Sigma-Aldrich	Cat#O1257
Palmitic acids	Sigma-Aldrich	Cat#P5585
Phosphoric acid	Sigma-Aldrich	Cat# P6560
PhosSTOP phosphatase inhibitor	Roche	Cat#4906837001
Protease inhibitor cocktail	Sigma-Aldrich	Cat#P8340
SPLASH® LIPIDOMIX mass spec standard	Avanti Polar Lipids	Cat#330707
Sucrose	Sigma-Aldrich	Cat#S9378
Tamoxifen	Sigma-Aldrich	Cat#T5648
Trizol	Life Technologies	Cat#15596026
TrueBlack	Biotium	Cat#23007
(Z)-4-hydroxytamoxifen	Sigma-Aldrich	Cat#H7904
U- <sup>13</sup> C-palmitate	Cambridge Isotope Laboratories	Cat#CLM4090.5
<b>Critical commercial assays</b>		
BCA protein assay kit	Thermo Fisher	Cat#23225
Free fatty acid assay kit	Abcam	Cat#ab65341
Triglyceride colorimetric assay kit	Cayman Chemical	Cat#10010303
<b>Deposited data</b>		
Lipidomics	This paper	Metabolomics Workbench: ST003644 (Project DOI: <a href="http://dx.doi.org/10.21228/M88J99">http://dx.doi.org/10.21228/M88J99</a> )
RNA-seq	This paper	GEO: GSE276591
Data S1. Source data	This paper	N/A
<b>Experimental models: Organisms/strains</b>		
Acly <sup>fl/fl</sup>	Zhao et al. <sup>28</sup> and Zhao et al. <sup>31</sup>	Acly <sup>fl/fl</sup> ; RRID: MMRC_043555-JAX
Acss2 <sup>fl/fl</sup>	Liu et al. <sup>34</sup>	Acss2 <sup>fl/fl</sup>
Acly <sup>fl/fl</sup> ; Acss2 <sup>fl/fl</sup>	Liu et al. <sup>34</sup>	Acly <sup>fl/fl</sup> ; Acss2 <sup>fl/fl</sup>
KRT14-CreER <sup>T</sup> ; Acly <sup>fl/fl</sup>	This paper	Acly <sup>ΔKRT14</sup>
KRT14-CreER <sup>T</sup> ; Acss2 <sup>fl/fl</sup>	This paper	Acss2 <sup>ΔKRT14</sup>
KRT14-CreER <sup>T</sup> ; Acly <sup>fl/fl</sup> ; Acss2 <sup>fl/fl</sup>	This paper	Acly <sup>ΔKRT14</sup> ; Acss2 <sup>ΔKRT14</sup>
KRT14-CreER <sup>T</sup> ; Adiponectin-Cre; Acly <sup>fl/fl</sup>	This paper	Acly <sup>ΔKRT14</sup> ; ΔADIPOQ
UBC-CreER <sup>T2</sup> ; Acly <sup>fl/fl</sup>	This paper	Acly <sup>ΔUBC</sup>
<b>Oligonucleotides</b>		
See Table S4	N/A	N/A
<b>Software and algorithms</b>		
ANY-maze	San Diego Instruments	Version 7.00
Bioconductor	Huber et al. <sup>88</sup>	Version 3.19
BioRender	BioRender	<a href="https://app.biorender.com/">https://app.biorender.com/</a>

(Continued on next page)

**Continued**

REAGENT or RESOURCE	SOURCE	IDENTIFIER
GSEA	Subramanian et al. <sup>89</sup>	Version 4.3.3
Illumina RNA-seq differential expression software (DESeq2)	Illumina	Version 1.0.1
Illumina RNA-seq alignment software	Illumina	Version 2.0.1
ImageJ (Fiji)	Schneider et al. <sup>90</sup>	Version 2.9.0/1.53t
LipidsSearch	Thermo Fisher	Version 5.0
MetaboAnalyst	MetaboAnalyst	Version 5.0
Prism	GraphPad	Version 10.4.0
R	R software	Version 4.4.2
RStudio	RStudio	Version 2024.04.2+764 for MacOS
<b>Other</b>		
Corn oil	Sigma-Aldrich	Cat#C8267
Olive oil	The Giant Company	N/A
Petroleum jelly	Covidien	Cat#8884430200
Tamoxifen-supplemented chow diet	Envigo	Cat#TD.130859
Zero-fat (62% sucrose) diet	Envigo	Cat#TD.03314

## EXPERIMENTAL MODEL AND STUDY PARTICIPANT DETAILS

### Animal studies

All animal studies were approved by the University of Pennsylvania (UPenn) Institutional Animal Care and Use Committee (IACUC). Mice were group-housed with littermates on a normal light-dark cycle (light on from 7 am to 7 pm) and fed rodent standard chow diet (LabDiet, 5010) ad libitum, except when special diets are indicated. Special diets were replaced bi-weekly for indicated lengths of time. The ambient temperature within the mouse housing facility was  $22^{\circ}\text{C} \pm 1^{\circ}\text{C}$ . Generation of *Acly*<sup>fl/fl</sup> mice have been previously described.<sup>28</sup> Exon 2 floxed *Acss2*<sup>f/+</sup> mice were generated using CRISPR/Cas9 on a C57Bl/6J background by the Viral Vector Core at the University of Iowa. *Acss2*<sup>fl/fl</sup> mice were generated by inter-breeding and selected by genotyping as described below.<sup>34</sup> Mice for *Acly* knockout experiments were generated by crossing *Acly*<sup>fl/fl</sup> mice with *UBC-CreER*<sup>T2</sup> mice<sup>91</sup> (kindly provided by Eric Brown), *KRT14-CreER*<sup>T</sup> mice<sup>92</sup> (kindly provided by Brian Capell), or *Adiponectin-Cre* mice.<sup>93</sup> Mice for experiments using double knockout (DKO) of *Acly* and *Acss2* were generated by crossing *Acly*<sup>fl/fl</sup> mice with *Acss2*<sup>fl/fl</sup> mice, then crossing the homozygous progeny with *KRT14-CreER*<sup>T</sup> mice. All mice were in C57Bl/6J background with at least 10 generations of back crosses. Mice used in experiments were 7–12 weeks old at the start of experiments, and experiments were conducted for up to 5 weeks, as indicated in text. Both male and female mice were used in all experiments unless otherwise indicated in figure legends.

### Human primary keratinocyte culture

Proliferating primary normal human epidermal keratinocytes (NHEKs) were isolated from deidentified discarded neonatal foreskin from male donors provided by the Skin Translational Research Core (STaR) of the Penn Skin Biology and Diseases Resource-based Center (SBDRC). NHEKs were cultured in a sterile filtered 50:50 mix of 1X keratinocyte serum-free medium (Thermo Fisher, 17005042) supplemented with human recombinant epidermal growth factor and pituitary extract combined with Medium 154 (Thermo Fisher, M154500) supplemented with human keratinocyte growth supplement (Thermo Fisher, S0015) and 1% of 10,000 U/mL antibiotic-antimycotic (Thermo Fisher, 15240062) at  $37^{\circ}\text{C}$  with 5% CO<sub>2</sub>. All proliferating NHEKs were cultured in NHEK medium under normal conditions. NHEKs used for experiments were between passages 5–7.

## METHOD DETAILS

### Inhibitor treatment and fatty acid supplementation for NHEKs

75,000 NHEKs were seeded in 6-cm dishes and allowed to adhere overnight before treatment in fresh NHEK media with 0.1% DMSO (Sigma-Aldrich, D2650) as vehicle control or 1 μM of BMS-30314 (ACLY inhibitor) (Tocris Bioscience, 4609) or in combination with 100 μM of palmitic acids (Sigma-Aldrich, P5585) and 100 μM of oleic acids (Sigma-Aldrich, O1257). Both fatty acids were conjugated to fatty-acid-free BSA (Bioworld, 22070023). Upon 24 hours of treatments, cells were collected by scraping in 1 mL of Trizol, flash frozen, and stored at -80°C.

**Genotyping**

Genotyping was performed in-house following previously published protocol.<sup>94</sup> Tail-snips from mice were digested in alkaline buffer (25 mM NaOH, 0.2 mM EDTA) on thermocycler at 95°C for 1 hour, cooled down, then neutralized by equal volumes of 40 mM Tris HCl. Genomic DNA samples were vortexed briefly and 2 µL was used for genotyping. *Acly*<sup>ff</sup> allele was confirmed with these primer sequences: Tm1c-F (AAG GCG CAT AAC GAT ACC AC); Tm1c-R (CCG CCT ACT GCG ACT ATA GAG A); *Acly*-null-R (CCT CTG AGC CAA TAT GCT CT); *Acly*-WT-F (TGC AAT GCT GCC TCC AAT GAT); *Acly*-WT-R (GGA GCC AGA GGA GAA AAA GGC); and the following cycling conditions: 1 cycle at 94°C for 2 minutes, 31 cycles at (94°C for 45 seconds, 58°C for 30 seconds, and 72°C for 30 seconds), 1 cycle at 72°C for 6 minutes and 40 seconds, hold at 4°C. *Acss2*<sup>ff</sup> allele was confirmed with these primer sequences: Acss2-F (GGA TAG TTA GCT TTG AGT ATA CAA GGA); Acss2-R (TCT CAA GAT ATC TGG CGT TGC); and the following cycling conditions: 1 cycle at 94°C for 3 minutes, 36 cycles at (94°C for 30 seconds, 60°C for 30 seconds, and 72°C for 1 minute), 1 cycle at 72°C for 10 minutes, and hold at 4°C. *UBC-CreER*<sup>T2</sup> allele was confirmed with these primer sequences: *UBC-CreER*<sup>T2</sup>-F (GAC GTC ACC CGT TCT GTT G); *UBC-CreER*<sup>T2</sup>-R (AGG CAA ATT TTG GTG TAC GG); and the following conditions: 1 cycle at 94°C for 2 minutes, 10 cycles at (94°C for 20 seconds, 65°C for 15 seconds with -0.5°C per cycle decrease, and 68°C for 10 seconds), 28 cycles at (94°C for 15 seconds, 60°C for 15 seconds, and 72°C for 10 seconds), 1 cycle at 72°C for 2 minutes, and hold at 10°C. *KRT14-CreER*<sup>T</sup> allele was confirmed with these primer sequences: *KRT14-CreER*<sup>T</sup>-F (CGC ATC CCT TTC CAA TTT AC); *KRT14-CreER*<sup>T</sup>-R (GGG TCC ATG GTG ATA CAA GG); and conditions described in genotyping of the *UBC-CreER*<sup>T2</sup> allele. *Adiponectin-Cre* allele was confirmed with these primer sequences: *ADIPOQ-Cre*-F (GGA TGT GCC ATG TGA GTC TG); *ADIPOQ-Cre*-R (ACG GAC AGA AGC ATT TTC CA); and conditions described in genotyping of the *UBC-CreER*<sup>T2</sup> allele.

**Tamoxifen regimen**

Each mouse was injected intraperitoneally with 100 µL of 20 mg/mL tamoxifen (Sigma-Aldrich, T5648) dissolved in corn oil (Sigma-Aldrich, C8267) using 0.5mL-27G syringes (Becton Dickinson, 305620) for 5 consecutive days (day 0-4). Then, standard chow diet was replaced with tamoxifen-supplemented chow diet (Envigo, TD.130859) on day 5 and reverted back to standard chow diet on day 12. Mouse body weight was monitored daily during tamoxifen injection and twice a week for the remaining time of experiments.

**Olive oil gavage**

Each mouse was given 200 µL of olive oil (The Giant Company) via oral gavage using 20G x 38mm feeding tubes (Fisher Scientific, 50-810-47) every other day, starting on day 12 post tamoxifen induction. Last gavage was given on day 20 (24 hours before tissue collection on day 21).

**Topical treatments**

To induce *Acly* knockout in the skin of *UBC-CreER*<sup>T2</sup>; *Acly*<sup>ff</sup> mice, 100 µL of 5 mg/mL of (Z)-4-hydroxytamoxifen (Sigma-Aldrich, H7904) dissolved in ethanol (Decon Laboratories, 2716) or 100 µL of vehicle control (100% ethanol) was pipetted directly and evenly onto 2 cm x 2 cm area of shaved dorsal skin for 5 consecutive days. For petroleum jelly treatment, mice were shaved in a 2 cm x 2 cm area on the dorsal side concurrent with starting tamoxifen induction, and a pea-size amount of petroleum jelly (Covidien, 8884430200) was applied evenly onto the shaved skin using cotton tip applicator (Puritan Medical, 25-806 2WC). Mice received this treatment daily for the entirety of the 5-week experiment.

**Metabolic cage and body composition analyses**

Metabolic cage and body composition analyses was performed by Penn IDOM Mouse Metabolic Phenotyping Core. Mice were individually housed in metabolic cages (Sable Systems, Promethion) and allowed to acclimate for 2 days before data recording. Recording was carried out for 7 days for the whole-body *Acly* knockout mice and 2 days for the skin-specific double knockout (DKO) of *Acly* and *Acss2* mice. Oxygen consumption (VO<sub>2</sub>) and carbon dioxide production (VCO<sub>2</sub>) were measured by indirect calorimetry every 5 minutes and used to calculate the respiratory exchange ratio (RER = VCO<sub>2</sub>/VO<sub>2</sub>) and energy expenditure using the Weir equation (Energy expenditure = 3.941 kcal/L x VO<sub>2</sub> + 1.106 kcal/L x VCO<sub>2</sub>).<sup>95</sup> Food intake and water intake were measured in the cages gravimetrically, and ambulatory activity was recorded through a beam break array. 24-hour data for each mouse was averaged from 7 days of recording and then mean of mice of each genotype was calculated. Body composition, including fat and lean mass, was measured with an EchoMRI 3-in-1 analyzer (EchoMRI, Houston, TX).

**Behavioral assessments**

Motor performance was evaluated by rotarod test according to previously published protocol<sup>96</sup> with modifications. Briefly, mice were placed on rotarod apparatus (Ugo Basile, model 47600) with accelerating mode (4-40 rpm) for 5 minutes. Each mouse was given 5 trials and 3 trials with longest retention time were averaged for the analysis. Hind limb clasping reflex was assessed by holding the mice upside down by the tail for 10 seconds and scoring manually according to the following metrics: 0-no clasping, 1-one limb retracts towards abdomen, 2-both limbs retract toward abdomen, 3-both limbs retract and touch the abdomen. Short-term memory test was evaluated by Y-maze (San Diego Instruments). Each mouse was given 3 minutes in 3-arm Y-maze and percent alternation

was calculated by dividing the correct alteration (visited 3 different arms sequentially) by the total number of alternations (visited any 3 arms) and multiplied by 100%. Long-term memory test was assessed by novel object recognition (NOR) test in multiple-unit open-field maze (San Diego Instruments) which consists of 4 chambers (Dimension: 50-cm length x 50-cm width x 38-cm height). On learning day, each mouse was placed into a chamber facing away from 2 identical objects and given 5 minutes to familiarize with those objects. After 24 hours, each mouse was placed into the same chamber with 1 familiar (from learning day) and 1 novel object. Number of entries into designated zones for both objects were divided by the total entries and multiplied by 100% to obtain discrimination index for each mouse. Both Y-maze and NOR tests were recorded by video camera and analyzed by automated tracking software (ANY-maze, version 7.00, San Diego Instruments).

#### **Glucose tolerance test**

Mice were individually housed and fasted for 6 hours. Body weight was used to calculate amount of D-glucose (Sigma-Aldrich, G8270) for a 2.0 g/kg given via oral gavage using 20G x 38mm feeding tubes (Fisher Scientific, 50-810-47). Glucose solution for gavage was prepared at concentration of 200 mg/mL using sterile PBS. Blood glucose was measured at time 0 after 6 hours of fasting and 20, 40, 60, and 120 minutes after the glucose gavage for each mouse.

#### **Tissue histology**

For hematoxylin and eosin (H&E) staining, tissues were fixed in formalin overnight, washed with PBS for 30 minutes, and dehydrated by titrating in ethanol (50% and 75%) and submitted to the Molecular Pathology and Imaging Core at the University of Pennsylvania for paraffin embedding, sectioning and staining. Quantifications of tissue histology was performed using ImageJ. For Oil-Red-O staining, tissues were fixed in 4% paraformaldehyde (Thermo Fisher, AAJ19943K2) overnight, dehydrated by 30% sucrose (Sigma-Aldrich, S9378) until completely submerged in solution, and frozen in plastic molds with optimal cutting temperature (OCT) embedding media (General Data Company, TFM-C). OCT-frozen tissues were submitted to the Molecular Pathology and Imaging Core at the University of Pennsylvania for cryo-sectioning and Oil-Red-O staining.

#### **Immunofluorescent staining**

Paraffin-embedded tissue sections were incubated at 60°C for 1 hour and rehydrated in the following series of solution for 5 minutes each: xylene x3, 100% ethanol, 95% ethanol, 70% ethanol, 50% ethanol, deionized water x2, and 1X PBS. Antigen retrieval was achieved by heating the tissue sections in citrate buffer (10 mM sodium citrate, 0.05% Tween 20, pH 6.0) and washed with PBS x2 for 5 minutes each. Tissue sections were outlined with a hydrophobic pen (Vector Laboratories, H-4000), washed with x3 with TBST (1X TBS containing 0.1% Tween-20, v/v) for 5 minutes each, and incubated in blocking solution (10% donkey serum, v/v; 0.5% Triton X-100, v/v; 1% BSS, w/v; 0.1% gelatin, w/v; 22.52 mg/mL glycine in TBST) for 1 hour at room temperature. Tissue sections were incubated with primary antibodies diluted 1:250 in antibody solution (5% donkey serum, v/v; 0.1% Triton X-100, v/v in TBST) overnight at 4°C. After washing in TBST x3 for 10 minutes each, the tissue sections were incubated with secondary antibodies diluted 1:500 in antibody solution described above for 1 hour at room temperature. Tissue sections were washed with TBST x3 for 5 minutes each. To reduce autofluorescence, tissues were washed with PBS for 5 minutes and incubated with TrueBlack reagent (Biotium, 23007) diluted 1:20 in 70% ethanol for 1 minute. After washing with PBS x2, slides were mounted with coverslips and mounting media (Vector Laboratories, H-1700-10), and sealed with clear nail polish. Antibodies used for immunofluorescent staining are listed in the [key resources table](#).

#### **Epidermal isolation**

Subcutaneous fat and some connective tissues were removed from 2 cm x 2 cm area of shaved dorsal skin by fine forceps and placed upside down in a 6-well plate containing ice-cold PBS. Scalpel was used to remove any visible fat residues from the skin. Skin samples were kept cold and submerged in PBS until other samples were ready for enzymatic dissociation of epidermis from dermis (maximum of 6 samples per batch). Fresh ice-cold 1X dispase solution was prepared from 10X (Corning, 354235) to achieve the final concentration of 5 U/mL in PBS. Skin samples were transferred upside up into a new 6-well plate, flattened out, and excess PBS gently dabbed away by Kimwipes. A corner of the skin section was lifted up by fine forceps and slowly added with 2 mL of 1X dispase for the skin section to be floating on the solution. There was less than 5 minutes in between floating the first and the last skin section in a batch. Skin sections floating on dispase solution were incubated at 37°C for 40 minutes or up to 1 hour until the epidermis was loosen from the dermis. Skin sections were then transferred onto a clean and dry surface, and excess enzymatic solution was removed by Kimwipes. Loose epidermis was scraped by clean spatula, collected into Eppendorf tubes, frozen in liquid nitrogen, and stored at -80°C.

#### **Western blotting**

Frozen tissues were homogenized in 0.5-1 mL RIPA buffer (1% NP-40, 0.5% deoxycholate, 0.1% SDS, 150 mM NaCl, 50 mM Tris) with protease inhibitor cocktail (Sigma-Aldrich, P8340) and PhosSTOP phosphatase inhibitor (Roche, 4906837001) using steel beads with Qiagen TissueLyser II for 1 minute at 30 Hz. Lysates were incubated on ice for 10 minutes after lysis, sonicated at 20% duty cycle for 15 seconds, then centrifuged at 15,000 g for 10 minutes at 4°C. Clear supernatant was collected and stored at -80°C. Protein concentration was measured with BCA protein assay kit (Thermo Fisher, 23225) per manufacturer's instruction.

20 µg of protein lysate was used for blotting with antibodies listed in the [key resources table](#). Western blots were developed using a LI-COR Odyssey Clx.

### Fecal protein extraction

Total fecal protein extraction was adapted from previously published protocol.<sup>97</sup> Frozen feces (10 mg) collected from individually housed mice were homogenized in 1 mL of lysis buffer (2% SDS, 150 nM NaCl, 0.5 M EDTA) using TissueLyser II, and protein concentration were measured as described for frozen tissue protein extraction above.

### RNA extraction

Frozen tissues (5–10 mg) were added to Eppendorf tubes containing steel beads and 1 mL of Trizol (Life Technologies, 15596026), homogenized using a Qiagen TissueLyser II for 1 minute at 30 Hz, followed by manufacturer's protocol for Trizol RNA extraction. For epidermal RNA extraction, frozen epidermis in 1 mL of Trizol was transferred to Lysing Matrix D (MP Biomedicals, 6913050) immediately after thawed, and homogenized by homogenizer (MP Biomedicals) x4 runs with 3-minute incubation on ice in between runs. Homogenates were centrifuged at 16,000 g for 5 minutes at 4°C and supernatants were transferred into new tubes. RNA was extracted with RNeasy Mini Kit (Qiagen, 74106) per manufacturer's instruction. RNA samples were stored at –80°C until further processing.

### RT-qPCR

High-capacity RNA-to-cDNA master mix (Applied Biosystems, 4368814) were used to synthesize cDNA as per manufacturer's instruction. cDNA was diluted 1:20 and amplified using PowerUp SYBR Green Master Mix (Applied Biosystems, A25778) on the ViiA-7 or QuantStudio 6 Pro Real-Time PCR system. Fold change in expression was calculated using the  $\Delta\Delta C_t$  method with corresponding housekeeping genes (*Gapdh* or *Actin* for mouse tissues, and *ACTIN* for primary human keratinocytes). Sequences for RT-qPCR primers are listed in [Table S4](#).

### RNA sequencing and analysis

RNA-seq libraries were prepared with the NEBNext poly(A) Magnetic Isolation Module (New England Biolabs, E7490L) followed by the NEBNext Ultra Directional RNA library preparation kit for Illumina (New England Biolabs, E7420L) according to manufacturer's protocol. Library quality was assessed using an Agilent BioAnalyzer 2100 and libraries were quantified with the Library Quant Kit for Illumina (New England Biolabs, E7630L). Libraries were then diluted to 1.8 pM and sequenced on the NextSeq500 platform using 75-base-pair (bp) single-end reads. All RNA-seq read alignment was performed using Illumina RNA-seq alignment software (version 2.0.1). Briefly, reads were mapped to *Mus musculus* University of California Santa Cruz (UCSC) mouse GRCm38/mm10 reference genome with RNA STAR aligner under default settings (version 2.6.1a).<sup>98</sup> Transcripts per million (TPM) generation and differential expression analysis was performed on aligned reads to *Mus musculus* UCSC GRCm38/mm10 reference genome using Illumina RNA-seq differential expression software (DESeq2, version 1.0.1).<sup>99</sup> Additional analyses were performed using R computing environment (version 4.4.2) and Bioconductor (version 3.19) in RStudio (version 2024.04.2+764 for MacOS) according to previously published code (<https://bioconductor.org/packages/release/bioc/html/EnhancedVolcano.html> and <https://bioconductor.org/packages/release/bioc/html/clusterProfiler.html>). Statistical significance was obtained using adjusted p-value (padj) and fold change cut offs indicated in the figure legends. The software for gene set enrichment analysis (GSEA) (version 4.3.3) was downloaded from the Broad Institute Molecular Signatures Database and GSEA and data was queried against Hallmark gene sets. Data are deposited in GEO under GSE276591.

### Trans epidermal water loss (TEWL)

Noninvasive probe for measuring subsurface-epidermal water content by diffusion (Tewameter TM300, Courage+Khazaka, Cologne, Germany) was used at the mouse experiment endpoint according to the manufacturer's instruction. TEWL measurements were taken from the dorsal skin and averaged at 1-second intervals for a 30-second period. During sampling and assessment, the mean indoor ambient temperature was 22.2°C (range = 18.3–23.9°C) and the mean relative humidity was 25.5% (range, = 16–68%).

### Thin layer chromatography (TLC)

For thin layer chromatography (TLC), lipids were extracted using frozen epidermis (5 mg) or serum (40 µL) and 2 mL of ice-cold methanol in 10 mL Pyrex Glass tubes, followed by 700 µL of ice-cold deionized water, then sonicated at 20% duty cycle for 15 seconds. The mixture was added with 1 mL of ice-cold chloroform and vortexed for 30 seconds. Additional 700 µL of ice-cold chloroform and 700 µL of ice-cold deionized water were added. The mixture was vortexed for 30 seconds and centrifuged at 2,000 rpm for 10 minutes at 4°C for phase separation. The bottom chloroform layer was transferred into a new glass tube to be dried under nitrogen gas overnight. Sebum lipids were extracted according to previously published protocol.<sup>63</sup> Briefly, hair (shaved from 2 cm x 5 cm in dorsal area) was transferred into 20 mL glass vial with 2:1 chloroform-methanol (v/v), sonicated for 6 minutes in portable water bath sonicator, and 1.6 mL was filtered into a 5 mL glass tube using polypropylene syringes (Millipore, Z683566) and 0.22 µm nylon filter (Thermo Fisher, CH2225-NN). 2 mL of acetone was added to wetted hair to further extract

lipids by 6-minute sonication. 1.6 mL of second extraction was filtered into glass tube which contained the first extraction. Total sebum extracts were dried under nitrogen gas overnight. Dried lipid weights were recorded before being resuspended in equal volumes of chloroform-methanol (4:1, v/v) for loading onto TLC plates (Sigma-Aldrich, 1.00390.0001). Lipid solution of 5  $\mu$ L (epidermal or sebum lipids) or 10  $\mu$ L (serum lipids) was spotted 1.5cm from the bottom of the TLC plate. TLC plates were then developed sequentially in the following solutions: (i) hexane:diisopropyl ether:glacial acetic acid (80:20:1, v/v) up to 50% of the plate height from the bottom, (ii) hexane:benzene (1:1, v/v) up to 90% of the plate height, and (iii) hexane up to 100% of the plate height. Plates were allowed to dry for 15 minutes between each solution. Plates were sprayed uniformly with a solution of 10% cupric sulfate (Sigma-Aldrich, 451657) and 8% phosphoric acid (Sigma-Aldrich, P6560), allowed to dry for 15 minutes, then baked at 120°C for 25 minutes to visualize lipid classes. Intensity of lipid classes was quantified by ImageJ. The non-polar lipid mixture 1 (Matreya, 1129) was used as standard to identify lipid classes.

### Fecal lipid extraction

For total fecal lipid extraction, 1 g of feces were collected from individually housed mice and lipids were extracted as described for TLC mouse epidermis. Lipids were dried under nitrogen gas overnight and weight was recorded.

### Lipid quantification by colorimetric assays

Total NEFAs in the mouse serum was quantified using free fatty acid assay kit (Abcam, ab65341). For measurement of triglycerides in sebum, dried sebum lipids were resuspended in 4:1 chloroform:methanol and a volume equivalent to 1 cm<sup>2</sup> of hair was dried down under N<sub>2</sub> gas before proceeding with triglyceride colorimetric assay kit (Cayman Chemical, 10010303). These assays were performed as per manufacturer's instructions.

### Lipidomics by liquid chromatography-high resolution mass spectrometry (LC-MS)

5 mg of frozen epidermis was homogenized in 0.6 mL of ice-cold 80% methanol using green bullet blender tubes (Next Advance NA-GREENR1-RNA) and the Next Advance Bullet Blender Tissue Homogenizer with dry ice at max speed x3 for 5 minutes each. The tubes were vortexed and allowed to settle and come to room temp for 30 minutes. 125  $\mu$ L of homogenate (equivalent to 1 mg of tissue) was transferred into a 10 mL Pyrex Glass tube, followed by adding 20  $\mu$ L of internal standard mix (1:1, SPLASH® LIPIDOMIX mass spec standard #330707: Ceramide/Sphingoid mixture I #LM6002, both from Avanti Polar Lipids), 80% methanol up to 2 mL of total methanol, and 1.7 mL of chloroform. The mixture was then shaken vigorously for 20 minutes at room temperature. Each sample was added with 1.4 mL of deionized water, vortexed for 30 seconds, and centrifuged at 2000 rpm for 10 minutes for phase separation. The bottom chloroform layer was collected and dried down under nitrogen gas. Then, dried lipids were resuspended in 200  $\mu$ L of methyl tert-butyl ether:methanol (1:3, v/v), sonicated for 5 minutes in water bath at room temperature, and centrifuged at 10,000 g for 10 minutes at 4°C. A pooled sample was made by mixing 40  $\mu$ L from each re-dissolved sample. This pooled sample was used as quality control (QC) for the LC-HRMS response and ran every 8 samples. The QC was used for data normalization. The rest of the lipid re-dissolved sample was transferred to a HPLC vial and 2  $\mu$ L injections were made in both positive mode and separately in the negative mode as previously described.<sup>82</sup> Control extraction blanks were made using only solvents instead of the tissue homogenate. The control extraction blanks were used for the exclusion list with a threshold feature intensity set at 1e10<sup>5</sup>. Untargeted analysis and targeted peak integration were performed using LipidsSearch (Thermo Fisher, version 5.0) as previously described.<sup>83</sup> An external mass calibration was conducted using the standard calibration mixture approximately every three days. All samples were analyzed in a randomized order in full scan MS (for quantification) that alternated with MS2 (for identification) of top 10, with HCD scans at 30, 45 or 60 eV. Heatmaps were generated with MetaboAnalyst (version 5.0).

### Quantification of fatty acids by fatty acid methyl-esterification (FAME) with gas chromatography-mass spectrometry (GC-MS)

Frozen epidermis (5 mg), sebum (from 2 cm x 5 cm hair in dorsal area) or serum (20  $\mu$ L) underwent similar lipid extraction for TLC as described above, except that 10  $\mu$ L of 1 mM U-<sup>13</sup>C-palmitate (Cambridge Isotope Laboratories, CLM4090.5) in ethanol was added to each sample as internal standard. To be derivatized into methyl-esters, dried lipids were resuspended in 2 mL of methanol:toluene (80:20, v/v) containing butylated-hydroxy toluene (0.1 mg/mL), added with 2  $\mu$ L of acetyl-chloride, and heated at 95°C for 1 hour. Samples were cooled to room temperature and 5 mL of 6% potassium carbonate was added. Samples were centrifuged at 2,000 rpm for 10 minutes at 4°C. The top toluene layer was transferred to an Eppendorf tube and centrifuged at 10,000 rpm for 5 minutes at room temperature. The final toluene was transferred into a glass gas chromatography-mass spectrometry (GC-MS) vial with a volume-reducing insert. Fatty acid methyl esters were analyzed by GC-MS on an Agilent GC-MS 7890A/5975A with a DB-5 column.

### T cell depletion and flow cytometry

To deplete T cells, each mice received rat IgG2b control (Bio X Cell, BE0090) or a cocktail of rat anti-CD4 (Bio X Cell, BE0003-1) and rat anti-CD8 $\alpha$  (Bio X Cell, BE0061) antibodies in PBS through intraperitoneal injections on day -2, 0, 5, 7, and 9 (day 0 was first TAM injection). Mouse blood was collected via tail bleed in heparin-coated tubes (Sarstedt, 16.443.100). To lyse red blood cells, Gibco™

ACK lysis buffer (Thermo Fisher, A1049201) was added to blood samples and incubated at 37°C for 15 minutes. PBS was used to neutralize ACK, and samples were then centrifuged for 5 minutes at 500g. Supernatant was discarded, and the pellet was resuspended in FACS buffer (1X PBS, 2% FBS, 1mM EDTA). Samples were stained with Ghost Dye™ Red 780 fixable viability dye (Cell Signaling Technology, 18452) in PBS 15 minutes at 4°C, then with Brilliant Violet 650™ anti-mouse CD4 (BioLegend, 100555), PE/Cyanine7 anti-mouse CD8 $\alpha$  (BioLegend, 100722), and Alexa Fluor® 700 anti-mouse CD45 (BioLegend, 103128), antibodies diluted in FACS buffer for 30 minutes at 4°C. After staining, cells were washed with FACS buffer, fixed in 2% paraformaldehyde for 10 minutes at 4°C, and resuspended in FACS buffer. Flow cytometry data was collected using an LSR II (BD) and analyzed using FlowJo (version 10.10).

#### **QUANTIFICATION AND STATISTICAL ANALYSIS**

Statistical analysis was done using GraphPad Prism. Student's t-tests or one- or two-way ANOVA with post-hoc Sidak's correction for multiple comparisons were used as indicated in figure legends.